Energy Engineering

Tech Science Press

Doi:10.32604/ee.2026.076436

ARTICLE

A Coordinated Control Strategy for SLCC Considering SVF Withstand Capability under Fault Conditions

Xintong Mao[1], Yechi Xu[1], Yaowen Sun[2], Zhihan Liu[1], Yumeng Wang[1] and Chuyang Wang[2,*]

[1]State Grid Jiangsu Electric Power Co., Ltd., Nanjing, China
[2]College of Electrical and Power Engineering, Hohai University, Nanjing, China
*Corresponding Author: Chuyang Wang. Email: wangchuyang@hhu.edu.cn

Received: 20 November 2025; Accepted: 05 January 2026; Published: 27 May 2026

ABSTRACT: The self-adaption STATCOM and line commutation converter (SLCC) system based on the static var generator and filter (SVF) utilizes the compensation capability of the SVF to reduce the commutation process's dependence on the AC grid, thereby enhancing the SLCC's ability to resist commutation failure. However, existing SLCC control strategies have not fully considered the boundary conditions for the safe and stable operation of the SVF (i.e., the SVF withstand capability), which limits or even deteriorates the ability of the SVF to provide commutation support for the SLCC under AC grid voltage fault conditions. To address this issue, this paper first analyzes the current and voltage limit boundaries of the SVF in the SLCC system from the perspective of SVF device stress, revealing the mechanism of SVF withstand capability exceedance under fault conditions. Based on this analysis, a voltage feedforward control strategy that accounts for the SVF withstand capability is proposed. This strategy accelerates the dynamic response of the SVF under fault conditions and enhances the SLCC's ability to resist commutation failure, while strictly avoiding the risks of SVF current and voltage exceedance, thereby ensuring the SVF operates within its withstand capability boundaries and improving support security under fault conditions. Furthermore, based on the SVF withstand capability boundaries, the commutation margin required to maintain safe commutation for the SLCC is calculated, and the SLCC inversion angle is dynamically adjusted accordingly. This achieves coordinated control between the SLCC and the SVF, preventing SVF blocking due to exceeding its withstand capability and ensuring safe commutation of the SLCC. Simulation results verify that the proposed strategy can simultaneously achieve non-blocking operation of the SVF and safe commutation of the SLCC.

KEYWORDS: SLCC; SVF withstand capability; coordinated control; commutation security

1 Introduction

In the field of high-voltage direct current (HVDC) transmission, two primary technologies exist: line commutated converter (LCC) and voltage source converter (VSC) [1]. Traditional LCC systems have been widely applied in engineering due to their advantages of large capacity and low losses [2,3]. However, with the increasing penetration of renewable energy, its randomness and volatility have led to the "hollowing-out" problem in the receiving-end AC grid [4], resulting in weakened grid support capability. Meanwhile, as the converter valves in LCCs use semi-controlled thyristors, the commutation process heavily relies on the AC grid to provide reactive power [5,6]. This drawback of LCCs will become more pronounced in future weak receiving-end grid scenarios, seriously threatening the stability and reliability of the power system [7]. Although VSC-HVDC technology demonstrates tremendous application potential in this scenario due to its control flexibility [8,9], its high cost leads to economic drawbacks [10,11]. To overcome the limitations of

conventional LCC while retaining its economic merits, it is essential to mitigate its dependence on voltage support from the AC grid for commutation during fault conditions. Inverter-based sources can provide such voltage support and, owing to their inherent DC-link capacitance, can deliver this support without additional hardware [12]. Therefore, they represent a viable solution for grid fault scenarios, even under severe imbalance conditions [13]. Following this rationale, the SLCC topology has been proposed [14]. The SLCC system connects an SVG or SVF in parallel to each branch of the LCC system. By utilizing the reactive power and harmonic compensation capabilities of the SVG or SVF, it reduces the reactive power exchange between the converter station and the AC grid, decreases the dependence of the LCC on the AC system, thereby enhancing system stability and reliability [14–16]. Furthermore, the voltage support capability of the SVF can accelerate the commutation process and reduce the risk of commutation failure.

Although SVF compensation can enhance the ability of the SLCC to resist commutation failure, in practical applications, the compensation capability of the SVF is limited by device stresses as it is composed of submodules using fully controlled devices, and cannot provide unlimited compensation. Especially when faults such as three-phase or single-phase voltage sags or ground faults occur in the AC system, the overcurrent in the LCC and voltage sags can impact the SVF, potentially causing excessive fluctuations in the SVF bridge arm current and submodule capacitor voltage, even exceeding the withstand capability of the devices, i.e., surpassing the current and voltage withstand capability boundaries of the SVF, thereby affecting its normal operation. Currently proposed control strategies for SLCC systems under fault conditions mainly adopt direct voltage feedforward [14] or constant voltage control with a limiter [15,16]. Both strategies use the converter valve bus voltage as the reference voltage, neglecting the withstand capability of the SVF. In cases of severe faults, this can easily lead to SVF blocking, increasing the risk of commutation failure to a level comparable to that of LCC systems, failing to fully utilize the voltage support role of the SVF, and making effective coordination between the SVF and LCC difficult.

To address the above issues, the main contributions of this paper are as follows:

(1) From the perspective of device stress, the current and voltage boundaries of the SVF in the SLCC system are analyzed, revealing the limitations of the SVF withstand capability in enhancing the SLCC's ability to resist commutation failure: although increasing the voltage support from the SVF can accelerate the commutation process and mitigate the risk of commutation failure, it may cause the SVF to block due to exceeding its withstand capability, consequently losing the enhancement it provides to the commutation margin of the SLCC.

(2) Based on the relationship between the SVF withstand capability boundaries and its voltage command value, a voltage feedforward control strategy considering the SVF withstand capability is proposed. This strategy uses the maximum voltage support that does not exceed the withstand capability as the feedforward command, accelerating the dynamic response of the SVF while strictly avoiding the risk of exceeding its withstand capability.

(3) Based on the SVF withstand capability boundaries, the commutation margin required to maintain safe commutation for the SLCC is calculated, and the SLCC inversion angle is dynamically adjusted accordingly. This achieves coordinated control between the LCC and the SVF, avoiding SVF blocking due to exceeding its withstand capability while maximizing its voltage support capability, and ensuring safe commutation of the SLCC system under fault conditions.

2 Principle of SLCC and Analysis of SVF Withstand Capability

2.1 Basic Working Principle of SLCC

The topological structure of the SLCC system is formed by connecting an SVF in parallel to each converter valve branch of the LCC system. Generally, the converter stations in an LCC system are typically composed of multiple six-pulse converter valves connected in series. The topological structure of each converter valve branch in the SLCC system and its existing operational control strategy are illustrated in Fig. 1. The meaning of each variable in this paper is provided in Table A1 in Appendix A.

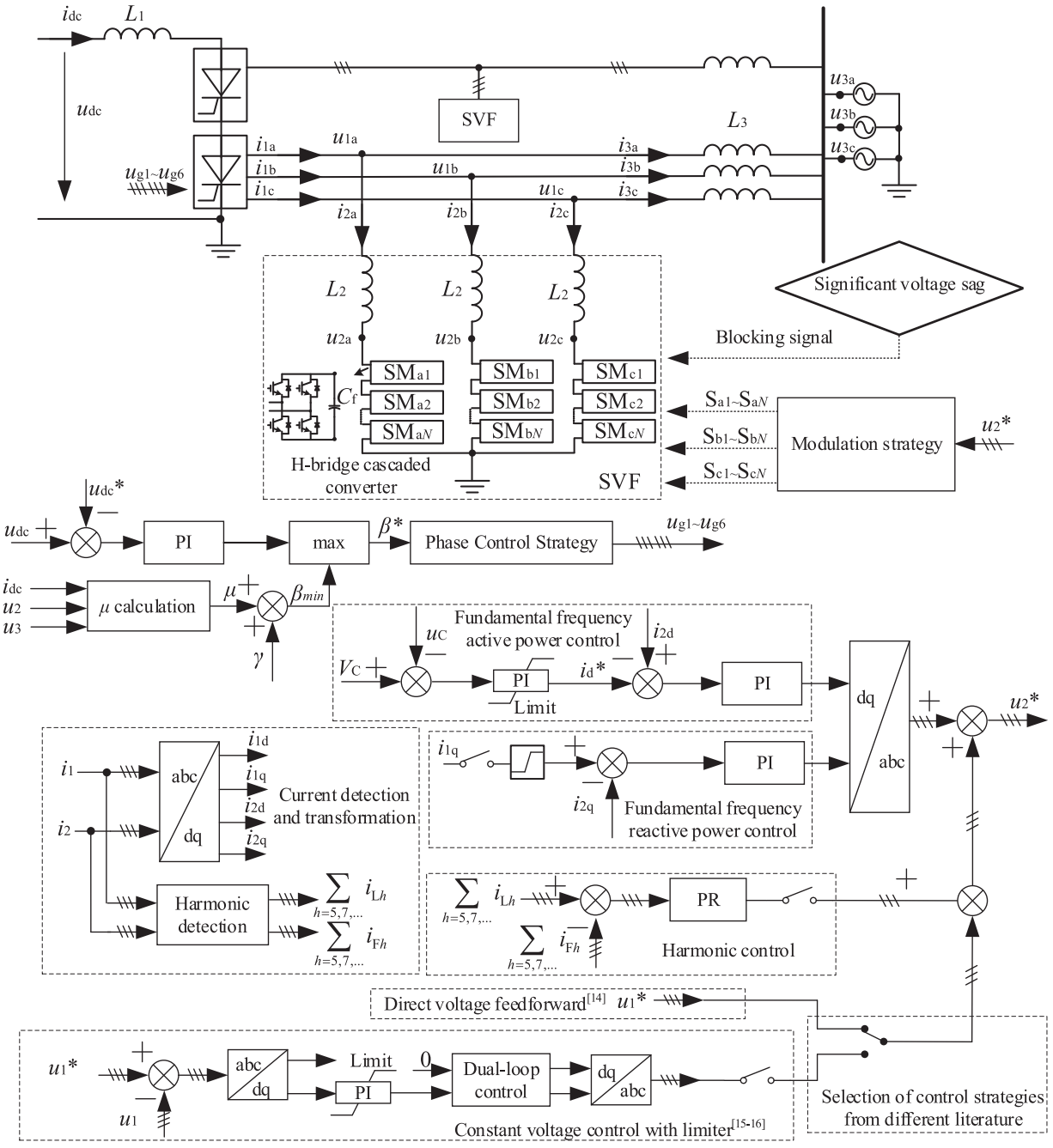

Figure 1: Overall structure of SLCC single-group converter valve and existing control strategies

As shown in Fig. 1, for each converter valve, the overlap angle μ is calculated based on the SVF's three-phase cascaded bridge voltage u_2, the grid three-phase voltage u_3, and the DC current i_{dc}. Through real-time measurement of the extinction angle γ, the minimum inversion angle β_{min} is obtained, thereby imposing boundary constraints on the thyristor phase control to maintain the balance between DC-side voltage and safe commutation.

For the SVF, during steady-state operation of the SLCC system, the active current command value i_d^* is derived from the difference between the submodule capacitor voltage rating V_C and the measured value u_C; the reactive current command value i_q^* is obtained from the difference between the reactive component i_{2d} in the converter valve line current and the reactive component i_{2q} in the SVF line current. These two components together form the fundamental frequency current control. Simultaneously, the harmonic control component is derived from the difference between the characteristic harmonic currents i_{Lh} of the LCC and the corresponding characteristic harmonic currents i_{Fh} in the SVF, constituting the harmonic current control. Finally, the above control components are synthesized with the voltage feedforward component to form the control voltage u_2^* for the SVF valve. When the SLCC system enters a fault condition, the fundamental frequency reactive power compensation and harmonic compensation are abandoned, and u_2^* is increased to enable the SVF to provide voltage support, thereby reducing the risk of commutation failure.

However, the SVF is composed of cascaded full-bridge submodules, and limited by IGBT device stress, cannot indefinitely increase u_2^* to provide voltage support. Particularly when a voltage sag fault occurs in the AC system, the overcurrent in the LCC and the voltage sag can impact the SVF. The specific relationship is illustrated in Fig. 2.

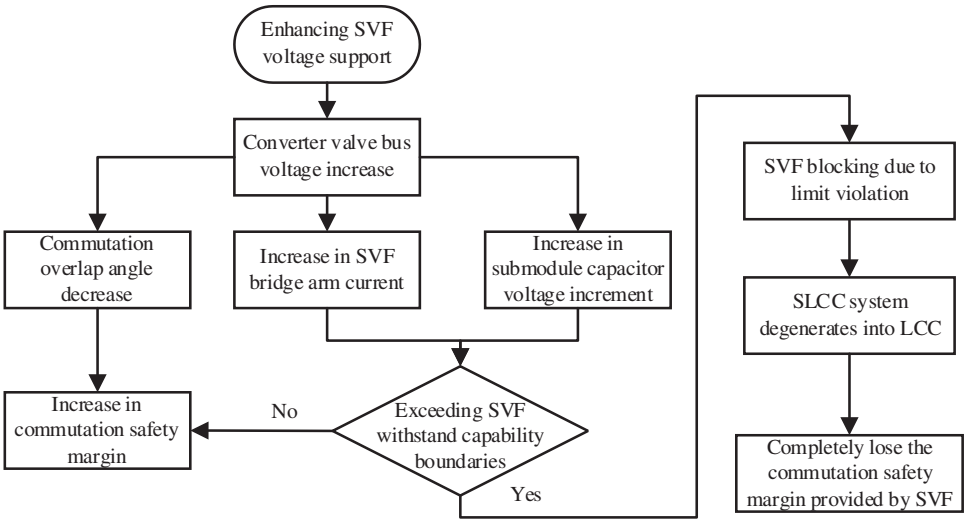

Figure 2: Schematic diagram of the relationship among SVF voltage support, system commutation safety margin, and SVF withstand capability

Therefore, the existing control strategy, which directly uses the converter station AC bus voltage command value u_1^* as the feedforward component [14], leads to SVF operation beyond its limits. Although the existing strategy can protect the SVF from damage through blocking, the SLCC system losing SVF voltage support degenerates back into an LCC system, failing to leverage the advantages of SLCC over LCC under fault conditions. On the other hand, the constant voltage control with a limiter sacrifices feedforward control to mitigate overlimit issues caused by rapid adjustment [15,16]. However, the added limiter and integral components prolong the control response time, making it incompatible with the requirement for the SVF to

rapidly provide voltage support during faults. Moreover, due to the lack of quantitative analysis of the SVF withstand capability, the limiter parameters rely on empirical settings, which may still lead to SVF blocking during severe voltage sags. Consequently, to better utilize the SVF's voltage support capability under fault conditions, it is essential to ensure that the SVF provides support without blocking. Thus, the design of control strategies requires analysis of the SVF's withstand capability boundaries under fault conditions.

2.2 Analysis of SVF Withstand Capability

2.2.1 Device Stress Limitation of the SVF

The SVF is composed of cascaded full-bridge submodule IGBTs, and its withstand capability is primarily constrained by the current and voltage limits of the submodule IGBTs, shown as Eq. (1).

$$\begin{cases} |i_2| \le I_{\text{permit}} \\ |\Delta u_{\text{C}}| \le \xi U_{\text{C}} \end{cases} \tag{1}$$

where, I_{permit} is the peak current boundary value triggering IGBT blocking in the SVF submodule, set based on the IGBT's maximum repetitive peak collector current I_{CRM} and incorporates an operational safety margin., i_2 is SVF three-phase bridge arm current, Δu_{C} represents the capacitor voltage increment of the SVF submodule, V_{C} stands for the rated capacitor voltage of the submodule, and ξ is the maximum allowable increase rate of the submodule capacitor voltage amplitude, set based on the capacitor's maximum allowable voltage ripple ratio and incorporates an engineering design margin. Both I_{permit} and ξ are determined by the device stress of the submodule itself.

2.2.2 Current Overlimit Boundary Condition of SVF

Assume that a voltage sag occurs at the receiving end of the system, leading to a fault condition. A single-phase branch (denoted as phase j, where j = a, b, c) is analyzed, and the voltage and current relationships can be derived based on the SLCC topology as shown in Eq. (2).

$$\begin{cases} u_{\text{dc}} - L_1 \dfrac{di_{\text{dc}}}{dt} = u_{2j} + L_2 \dfrac{di_{2j}}{dt} = u_{3j} + L_3 \dfrac{di_{3j}}{dt} \\ i_{\text{dc}} = i_{2j} + i_{3j} \end{cases} \tag{2}$$

where u_{dc} is the DC side voltage, i_{dc} denotes the DC side current, i_{2j} represents the j-phase line current of the SVF, i_{3j} stands for the j-phase line current of the grid, L_1 is the DC side inductor, L_2 is the SVF inductor, L_3 is the grid-side equivalent inductance, representing the sum of the equivalent inductances of the line and transformer between the receiving-end grid voltage bus and the SVF coupling point (primarily the transformer leakage inductance), u_{2j} is the j-phase cascaded bridge voltage of the SVF, and u_{3j} represents the j-phase grid voltage.

Rearranging and approximating Eq. (2) (considering $L_3 << (1 + L_3/L_2)L_1$), the rate of change of the DC current i_{dc} can be obtained as Eq. (3).

$$\begin{aligned} \frac{di_{\text{dc}}}{dt} &= \frac{u_{\text{dc}}\left(1 + L_3/L_2\right) - u_{2j}L_3/L_2 - u_{3j}}{\left(1 + L_3/L_2\right)L_1 + L_3} \\ &\approx \frac{u_{\text{dc}}\left(1 + L_3/L_2\right) - u_{2j}L_3/L_2 - u_{3j}}{\left(1 + L_3/L_2\right)L_1} \\ &= \frac{u_{\text{dc}}}{L_1} - \frac{u_{2j}L_3/L_2 + u_{3j}}{\left(1 + L_3/L_2\right)L_1} \end{aligned} \tag{3}$$

Substituting Eq. (3) back into Eq. (2), the rate of change of the j-phase arm current i_{2j} can be obtained as Eq. (4).

$$\frac{di_{2j}}{dt} = \frac{1}{L_2}u_{\mathrm{dc}} - \frac{1}{L_2}u_{2j} - \frac{L_1}{L_2}\frac{di_{\mathrm{dc}}}{dt} = \frac{-1}{L_2+L_3}u_{2j} + \frac{1}{L_2+L_3}u_{3j} \tag{4}$$

Integrating both sides of Eq. (4) yields Eq. (5)

$$i_{2j} = \frac{1}{L_2+L_3}\int \left(u_{3j} - u_{2j}\right)dt + \frac{L_3}{L_2+L_3}i_{\mathrm{dc}} \tag{5}$$

Assume that an AC fault manifests as a sag in the grid three-phase bus voltage. Simultaneously, neglecting the high-frequency components generated by SVF modulation, u_{2j} and u_{3j} can be expressed as Eq. (6):

$$\begin{cases} u_{2j} = \left(1 + \dfrac{N_{\mathrm{sub}}\Delta u_{\mathrm{c}}}{u_{\mathrm{dc}}}\right)U_2 \sin\left(\omega_0 t + \varphi_{\mathrm{u}2j}\right) \\ u_{3j} = \eta_j U_3 \sin\left(\omega_0 t + \varphi_{\mathrm{u}3j}\right) \\ \varphi_{\mathrm{u3a}} = 0 \\ \varphi_{\mathrm{u3b}} = -\frac{2}{3}\pi \\ \varphi_{\mathrm{u3c}} = \frac{2}{3}\pi \end{cases} \tag{6}$$

where N_{sub} is the number of submodules put into operation, U_2 is the voltage amplitude of the three-phase cascaded bridge of the SVF, η_j is the voltage sag severity of the j-th phase in the receiving-end AC system, U_3 is the voltage amplitude of the three-phase grid, and ω_0 is the angular frequency of the grid voltage. $\varphi_{\mathrm{u}3j}$ is the phase angle of grid j-phase phase voltage. $\varphi_{\mathrm{u}2j}$ is the phase angle of SVF j-phase cascaded bridge voltage.

Substituting Eq. (5) and rearranging yields the SVF bridge arm current expression as Eq. (7).

$$\begin{aligned} i_{2j} &= \frac{1}{L_2+L_3}\int \left[\eta_j U_3 \sin\left(\omega_0 t\right) - \left(1 + \frac{N_{\mathrm{sub}}\Delta u_{\mathrm{c}}}{u_{\mathrm{dc}}}\right)U_2 \sin\left(\omega_0 t + \varphi_{\mathrm{u}2j}\right)\right]dt + \frac{L_3}{L_2+L_3}i_{\mathrm{dc}} \\ &\approx \sqrt{\left[-\frac{1}{\omega_0\left(L_2+L_3\right)}\eta_j U_3 + \frac{1}{\omega_0\left(L_2+L_3\right)}U_2\cos\left(\varphi_{\mathrm{u}2j}\right)\right]^2 + \left[\frac{1}{\omega_0\left(L_2+L_3\right)}U_2\sin\left(\varphi_{\mathrm{u}2j}\right)\right]^2}\sin\left(\omega_0 t + \varphi\right) \\ &\quad + \frac{L_3}{L_2+L_3}i_{\mathrm{dc}} \end{aligned} \tag{7}$$

where ΔU_2 is the amplitude of the submodule capacitor voltage, and φ_{uc} is the phase angle of the submodule capacitor voltage. φ is a synthesized angle in the derivation process, and its specific calculation expression, along with the complete derivation of Eq. (7), is provided in Appendix B.1.

The amplitude of the j-phase bridge arm current of the SVF, $|i_{2j}|$, can be derived as Eq. (8).

$$\left|i_{2j}\right| = \sqrt{\left[-\frac{1}{\omega_0\left(L_2+L_3\right)}\eta_j U_3 + \frac{1}{\omega_0\left(L_2+L_3\right)}U_2\cos\left(\varphi_{\mathrm{u}2j}\right)\right]^2 + \left[\frac{1}{\omega_0\left(L_2+L_3\right)}U_2\sin\left(\varphi_{\mathrm{u}2j}\right)\right]^2} + \frac{L_3}{L_2+L_3}i_{\mathrm{dc}} \tag{8}$$

where $\varphi_{\mathrm{i}1j}$ is the phase angle of the j-phase line current of the converter valve, and $\varphi_{\mathrm{u}2j}$ is the phase angle of the j-phase cascaded bridge voltage of the SVF.

A three-dimensional diagram of $|i_{2j}|$ vs. (i_{dc}, U_2) is plotted according to Eq. (8), as shown in Fig. 3. SLCC system parameters are shown in Table 1.

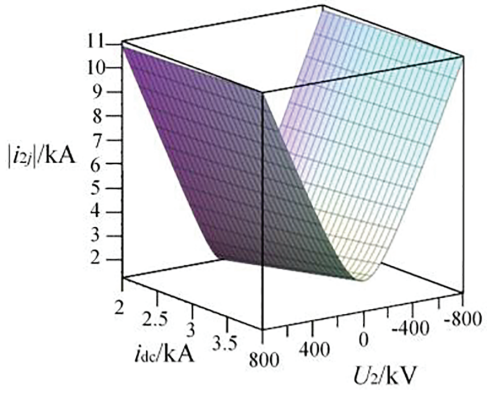

Figure 3: Relationship among the SVF bridge arm current amplitude $|i_{2j}|$, the DC current i_{dc}, and the SVF voltage U_2

Table 1: SLCC system parameters

Parameter	Value
AC system voltage (RMS)/kV	132
Grid voltage frequency/Hz	50
DC current/A	3000
DC voltage/kV	200
Active power/MW	600
DC-side inductance/mH	250
SVF bridge arm inductance/mH	8.5
Grid-side inductance/mH	15
Number of submodules	72
SVF submodule capacitance/mF	13
SVF submodule rated voltage/kV	2.8
IGBT maximum allowable current/A	4700
Maximum repetitive peak collector current I_{CRM}	6000
ξ	0.26
Submodule maximum allowable capacitor voltage/V	3640
Maximum capacitor voltage setting for submodule/V	3520
Extinction angle γ/°	5
Minimum margin angle θ_{min}/°	10

As shown in Fig. 3, an increase in U_2 leads to a sharp increase in $|i_{2j}|$, causing the SVF current to exceed its limit. When the system operates under a fault condition, the rise in DC current i_{dc} exacerbates the variation in the SVF bridge arm current amplitude. If the SVF voltage U_2 is not limited, $|i_{2j}|$ will exceed 10 kA when i_{dc} rises to 4 kA, imposing excessive demands on the current withstand capability of the SVF.

To demonstrate the validity of the approximation used in Eq. (8), the calculated and simulated values under several fault conditions are compared, as shown in Table 2.

Table 2: The calculated and simulated values of SVF bridge arm current under several fault conditions

Fault condition	One-phase voltage sags to 0.3 p.u.	One-phase voltage sags to 0.8 p.u.	Three-phase voltage sags to 0.8 p.u.
i_{dc}/A	7835	3828	4627
u_{2j}/V	55,669	101,836	103,780
$\lvert i_{2j}\rvert$ (Calculation results)	5213	2894	3408
$\lvert i_{2j}\rvert$ (Simulation results)	5093	2776	3039
Error/A	120	118	369
Relative Error	2.36%	4.25%	5.22%

2.2.3 SVF Voltage Limit Boundary Condition

Similarly, assuming a voltage sag occurs at the receiving end of the system, entering a fault condition, and still taking phase j as an example, the SVF capacitor voltage increment can be obtained as Eq. (9).

$$\Delta u_C = \frac{1}{C_f}\int i_C dt = \frac{1}{N_{sub}C_f}\int \frac{u_{2j}}{u_C}\cdot i_{2j}dt \tag{9}$$

where i_C is the submodule capacitor current, N_{sub} is the number of submodules put into operation, u_{2j} is the j-phase cascaded bridge voltage of the SVF, and C_f is the capacitance of a single submodule.

Substituting Eq. (7) into (9), yields Eq. (10).

$$\Delta u_C \approx \frac{1}{N_{sub}C_f}\int \frac{U_2\sin\left(\omega_0 t+\varphi_{u2j}\right)}{u_C}\cdot\left[\sqrt{\begin{bmatrix}-\dfrac{1}{\omega_0\left(L_2+L_3\right)}\eta_j U_3\\ +\dfrac{1}{\omega_0\left(L_2+L_3\right)}U_2\cos\left(\varphi_{u2j}\right)\end{bmatrix}^2+\left[\frac{1}{\omega_0\left(L_2+L_3\right)}U_2\sin\left(\varphi_{u2j}\right)\right]^2}\sin\left(\omega_0 t+\varphi\right)+\frac{L_3}{L_2+L_3}i_{dc}\right]dt \tag{10}$$

By organizing and approximating, Eq. (11) can be obtained; the detailed derivation is provided in Appendix B.2.

$$\begin{cases}\Delta u_C = \dfrac{U_2}{N_{sub}C_f u_C}\displaystyle\int\left\{B\cos\left(\varphi_{u2j}-\varphi\right)-B\cos\left(2\omega_0 t+\varphi_{u2j}+\varphi\right)+\frac{L_3}{L_2+L_3}i_{dc}\sin\left(\omega_0 t+\varphi_{u2j}\right)\right\}dt\\ \quad\approx \dfrac{-1}{N_{sub}C_f}\dfrac{U_2L_3}{\left(L_2+L_3\right)u_C\omega_0}\cos\left(\omega_0 t+\varphi_{u2j}\right)i_{dc}\\ B=\dfrac{1}{2}\sqrt{\left[-\dfrac{1}{\omega_0\left(L_2+L_3\right)}\eta_j U_3+\dfrac{1}{\omega_0\left(L_2+L_3\right)}U_2\cos\left(\varphi_{u2j}\right)\right]^2+\left[\dfrac{1}{\omega_0\left(L_2+L_3\right)}U_2\sin\left(\varphi_{u2j}\right)\right]^2}\end{cases} \tag{11}$$

Thus, the amplitude of the SVF capacitor voltage increment is as Eq. (12).

$$\lvert\Delta u_c\rvert \le \frac{1}{N_{sub}C_f}\cdot\frac{U_2L_3}{\left(L_2+L_3\right)u_C\omega_0}i_{dc} \tag{12}$$

Since the SVF submodule voltage u_C generally stabilizes at the rated value V_C during steady-state operation, to intuitively illustrate the relationship among $|\Delta u_C|$, i_{dc} and U_2, while maintaining u_C at its rated value, a three-dimensional diagram of $|\Delta u_C|$ vs. (i_{dc}, U_2) is plotted according to Eq. (12), as shown in Fig. 4.

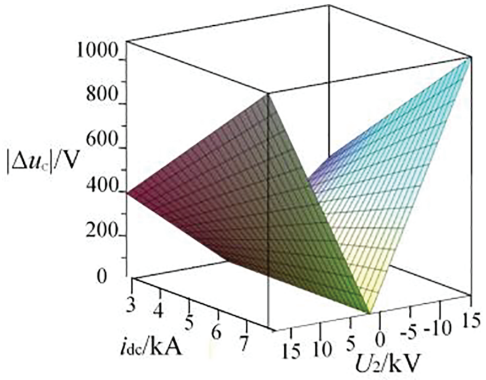

Figure 4: Relationship among the submodule capacitor voltage increment amplitude $|\Delta u_C|$, the DC current i_{dc}, and the SVF voltage U_2

As shown in Fig. 4, an increase in U_2 also leads to an increase in $|\Delta u_C|$. If u_C operates at the rated value during steady state, the submodule capacitor voltage increment will exceed 400 V when the DC current i_{dc} rises to 4.5 kA and the SVF voltage reaches 1.25 kV. When i_{dc} rises to 7 kA and U_2 reaches 1.5 kV, $|\Delta u_C|$ will exceed 900 V. It can be predicted that if the SVF voltage U_2 is not limited, the SVF voltage will further increase to support the commutation voltage as the fault severity intensifies, causing $|\Delta u_C|$ to exhibit even larger values, and a further rise in i_{dc} will exacerbate this issue. Therefore, if the converter valve bus voltage command value u_1^* is directly used as the feedforward quantity without limitation, the SVF will block due to exceeding its voltage withstand capability boundary under severe fault conditions.

To demonstrate the validity of the approximation used in Eq. (12), the calculated and simulated values under several fault conditions are compared, as shown in Table 3.

Table 3: The calculated and simulated values of SVF submodule capacitor voltage increment under several fault conditions

Fault condition	One-phase voltage sags to 0.3 p.u.	One-phase voltage sags to 0.8 p.u.	Three-phase voltage sags to 0.8 p.u.
i_{dc}/A	7835	3828	4627
u_{2j}/V	55,669	101,836	103,780
Δu_C (Calculation results)	338	302	372
Δu_C (Simulation results)	320	283	336
Error/V	18	19	36
Relative Error	5.62%	6.71%	10.71%

3 Design of SLCC System Coordinated Control Strategy

The key to the normal operation of the DC transmission system lies in the safe commutation of the converter valves [17,18]. The condition is Eq. (13).

$$\begin{cases} \pi - \alpha = \beta \geq \beta_{min} = \gamma + \mu \\ \beta = \beta_{min} + \theta \end{cases} \tag{13}$$

where α is the firing angle of the converter station, μ is the overlap angle, γ is the extinction angle (corresponding to the thyristor turn-off time converted to an electrical angle), β is the inversion angle, also known as the advance firing angle, and $\beta_{\min}$ is the minimum inversion angle. In practical operation, a margin angle θ is often intentionally added, setting the inversion angle command value to the sum of $\beta_{\min}$ and θ to address issues caused by fluctuations. Clearly, the maximum value of θ is the difference between β and $\beta_{\min}$, serving as a measure of the commutation safety margin.

In traditional LCC systems, the commutation process relies on the AC grid voltage to transfer current from one valve to another. Therefore, when a voltage sag occurs in the AC grid, the overlap angle increases [19]. Since γ is determined by the device's own characteristics [20,21] and cannot be directly controlled, the method usually adopted to avoid commutation failure is to increase β, i.e., decrease α. However, this approach causes the transmitted power to decrease rapidly, affecting the rotor angle stability of the AC system. Consequently, to avoid excessive adjustment of β, traditional LCC systems typically calculate μ based on the current voltage sag situation, compute the minimum inversion angle $\beta_{\min}$ required to avoid commutation failure based on this, and then control the command value of α (or β) of the converter station [22].

By analogy with the LCC commutation process [23], the equivalent circuit of the SLCC system commutation process can be derived, as shown in Fig. 5.

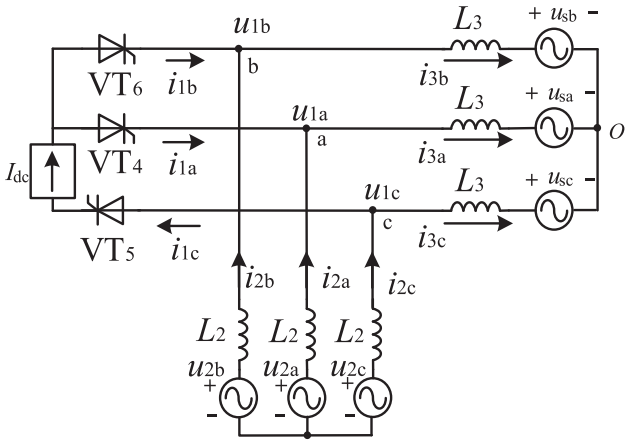

Figure 5: Equivalent circuit diagram of the SLCC system commutation process

Based on the equivalent circuit, equations are formulated and solved, yielding the following relationship as Eq. (14):

$$i_{\mathrm{dc}} = -\frac{\sqrt{3}}{2\omega_0 L_2 L_3}\left\{U_3 L_2\left[\cos\left(\alpha+\mu\right)-\cos\left(\alpha\right)\right]+U_2 L_3\left[\cos\left(\alpha+\varphi_{\mathrm{u}2j}+\mu\right)-\cos\left(\alpha+\varphi_{\mathrm{u}2j}\right)\right]\right\} \tag{14}$$

An approximation is performed on Eq. (14) to simplify the calculation, yielding Eq. (15). The complete derivation is provided in Appendix B.3.

$$\mu \approx \arcsin \frac{I_{\mathrm{dc}}}{\frac{\sqrt{3}}{2\omega_0}\left[\frac{U_3}{L_3}\sin\left(\alpha\right)+\frac{U_2}{L_2}\sin\left(\alpha+\varphi_{\mathrm{u}2j}\right)\right]} \tag{15}$$

From Eq. (15), increasing U_2 can accelerate the commutation process and improve the commutation margin. This is precisely why existing SLCC control strategies aim for the SVF to rapidly provide voltage support under fault conditions.

However, according to Eqs. (8) and (12), providing voltage support by the SVF causes an increase in its bridge arm current amplitude $|i_{2j}|$ and the submodule capacitor voltage increment amplitude $|\Delta u_C|$. When the fault severity intensifies, the SVF may exceed its withstand capability limits. This leads to the existing SLCC control strategy, which uses the converter valve bus voltage directly as feedforward, causing the SVF to block when fault severity increases due to exceeding its limits. Consequently, the SLCC system degenerates into an LCC system when the receiving-end grid voltage sags significantly, making the system rely entirely on the adjustment of the inversion angle to maintain safe commutation, or even leading to shutdown. Therefore, to fully utilize the SVF's ability to improve the system's commutation margin under fault conditions, the voltage feedforward compensation for the SVF should be corrected according to its withstand capability boundary conditions, adjusting the feedforward coefficient.

Since the three-phase cascaded bridge voltage of the SVF is the control variable, let the command value of the SVF's three-phase cascaded bridge voltage be u_2^*, its amplitude be U_2^*, and its phase angle be φ_{u2j}^*. Combining Eqs. (1) and (8) yields the SVF current withstand capability boundary condition as Eq. (16).

$$\begin{aligned}|i_{2j}| = &\sqrt{\left[\begin{array}{l}-\dfrac{1}{\omega_0\left(L_2+L_3\right)}\eta_j U_3 \\ +\dfrac{1}{\omega_0\left(L_2+L_3\right)}U_2\cos\left(\varphi_{u2j}\right)\end{array}\right]^2+\left[\frac{1}{\omega_0\left(L_2+L_3\right)}U_2\sin\left(\varphi_{u2j}\right)\right]^2\sin\left(\omega_0 t+\varphi\right)} \\ &+\frac{L_3}{L_2+L_3}i_{dc}\le I_{permit}\end{aligned} \tag{16}$$

Thus, the voltage feedforward compensation boundary to avoid SVF bridge arm current and submodule capacitor voltage exceeding limits is obtained as Eq. (17).

$$U_2^*\le\eta_j U_3\left[\cos\left(\varphi_{u2j}\right)+\sqrt{-\sin^2\left(\varphi_{u2j}\right)+\frac{{\omega_0}^2\left(L_2+L_3\right)^2\left(I_{permit}-\dfrac{L_3}{L_2+L_3}i_{dc}\right)^2}{{\eta_j}^2{U_3}^2\sin^2\left(\omega_0 t+\varphi\right)}}\right]=V_{m1} \tag{17}$$

In Eq. (17), V_{m1} is the feedforward voltage boundary generated due to the SVF submodule current limit.

Similarly, combining Eqs. (1) and (12) yields the SVF voltage limit boundary condition as Eq. (18).

$$|\Delta u_C|\le\frac{1}{N_{sub}C_f}\cdot\frac{U_2L_3}{\left(L_2+L_3\right)u_{dc}\omega_0}i_{dc}\le\xi U_c \tag{18}$$

Thus, the voltage feedforward compensation boundary for the submodule capacitor voltage limit is obtained as Eq. (19).

$$U_2^*\le\frac{\left(L_2+L_3\right)C_f u_{dc}\omega_0 N_{sub}\xi U_c}{L_3 I_{dc}}=V_{m2} \tag{19}$$

In the equation, V_{m2} is the feedforward voltage boundary generated due to the SVF submodule voltage limit. To avoid SVF blocking while exerting its maximum voltage support capability, the feedforward coefficient K_v should be set as Eq. (20).

$$K_v = \frac{\min(V_{m1}, V_{m2}) - U_2}{U_3} \tag{20}$$

Under this feedforward coefficient setting, the SVF will provide the maximum voltage support that does not exceed its withstand capability under fault conditions. Obviously, compared to the steady-state condition, there is a shortfall in this voltage support. When the fault severity increases, to compensate for the supporting effect of this voltage shortfall on the commutation process, it is still necessary to increase the converter station inversion angle. To fully leverage the flexible regulation capability of the SVF, this paper proposes a coordinated control strategy between the SVF and the LCC under AC system faults, as shown in Fig. 6. Besides, in practical applications, due to component nominal tolerances, a safety factor can be introduced to modify Eq. (20) the specific setting method is provided in Appendix C.

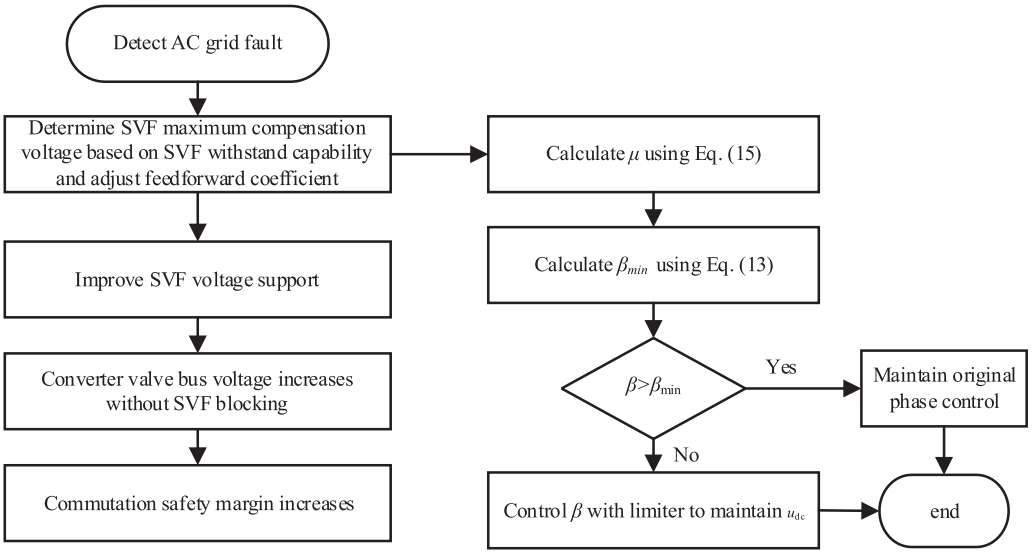

Figure 6: Coordinated control strategy between SVF and LCC in the SLCC system under fault conditions

In Fig. 6, the strategy first detects the AC system voltage, based on which the overlap angle of the thyristors is calculated. If a commutation failure risk is identified, the feedforward coefficient is calculated and adjusted according to the SVF withstand capability. At this time, since the SVF's three-phase cascaded bridge voltage command value u_2^* is limited within its maximum safe compensation voltage range, u_2^* can be directly used as the SVF's maximum compensation voltage. Combined with the receiving-end AC system voltage u_3 under fault conditions, the SLCC overlap angle is calculated using Eq. (15).

Next, if the SLCC meets the safe commutation condition under the SVF's maximum output voltage, the SLCC inversion angle remains unchanged to avoid frequent switching of the SLCC and increased reactive power consumption. If there is still a risk of commutation failure, then based on the angle shortfall for safe commutation, a lower limiter should be added to the inversion angle control process to avoid commutation failure. The control strategy for SLCC under fault conditions, as presented in Fig. 1, is improved by replacing the corresponding control module with the method illustrated in Fig. 6. Thus, this paper proposes the SLCC feedforward coordinated control strategy based on angle limiting, as shown in Fig. 7.

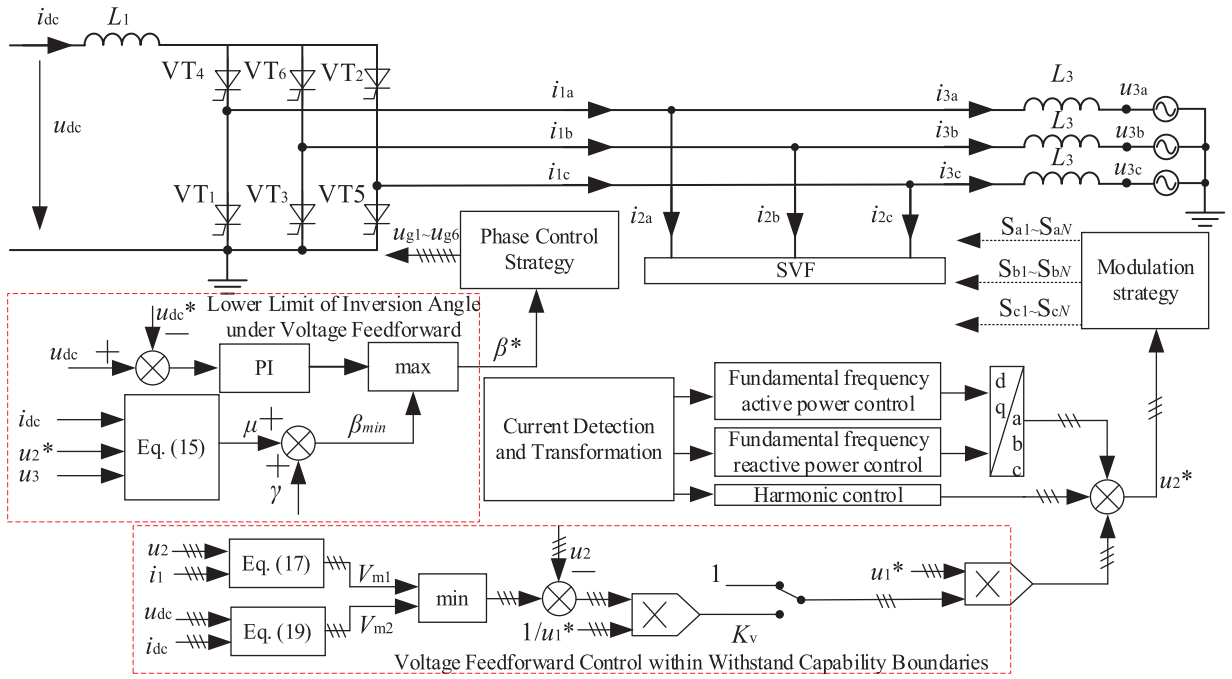

Figure 7: SLCC feedforward coordinated control strategy based on angle limiting

In this control strategy, the steady-state control strategy is consistent with existing strategies: the SVF sets the reactive power command according to the reactive power demand of the system during LCC operation, and sets the harmonic command according to the characteristic harmonics of the LCC (characteristic orders are $6nk \pm 1$, where n is the number of series-connected six-pulse converter valves in a single converter station, k = 1, 2, 3, ...), controlling the SVF to provide reactive power and harmonic compensation for the LCC, respectively. The LCC adjusts the inversion angle according to the steady-state operating conditions to maintain safe commutation of the converter station.

When a fault occurs on the AC side of the SLCC, the SVF abandons fundamental frequency reactive power control and harmonic control, switching to voltage feedforward control under fault conditions. As the SLCC control system incorporates a high-speed DSP and a large-scale FPGA, abundant computational resources are available. Consequently, the voltage feedforward boundaries that do not exceed the SVF's withstand capability are computed online based on real-time measurements according to Eqs. (17) and (19), and the feedforward coefficient is adjusted to achieve maximum voltage support under the constraint of avoiding SVF blocking. Based on the amount of voltage support provided by the SVF, the voltage shortfall for maintaining safe commutation is calculated, and the lower limit of the converter station inversion angle is adjusted to ensure safe commutation.

However, when the voltage sag further intensifies, even with the SVF providing the maximum voltage support under the boundary conditions, the required increase in the inversion angle to maintain safe commutation would still be excessively large. Under such circumstances, sustaining the SLCC system becomes impractical. Therefore, it is preferable to deactivate the SVF, allowing the system to degenerate into LCC operation. The transition conditions between these different operating modes are illustrated in Fig. 8.

As shown in Fig. 8, the control strategy operates as follows: when all three-phase voltages of the AC grid are above 0.8 p.u., the voltage support provided by the SVF alone ensures an adequate commutation safety margin, making it unnecessary to reduce the inversion angle. In the event of multiple-phase voltage

sags reaching 0.3 p.u. in the AC grid, the SVF is blocked. For all other conditions, the system employs the coordinated feedforward control strategy with angle limiting. A hysteresis band is applied to prevent mode chattering near the critical boundaries: for instance, the system will remain in the LCC mode until a recovery condition (multiple-phase voltages above 0.4 p.u. sustained for 20 ms) is met. This fully leverages the advantage of the SVF's flexible adjustment, maximizes the utilization of the SVF's voltage support capability, and ensures the safe and stable operation of the DC system.

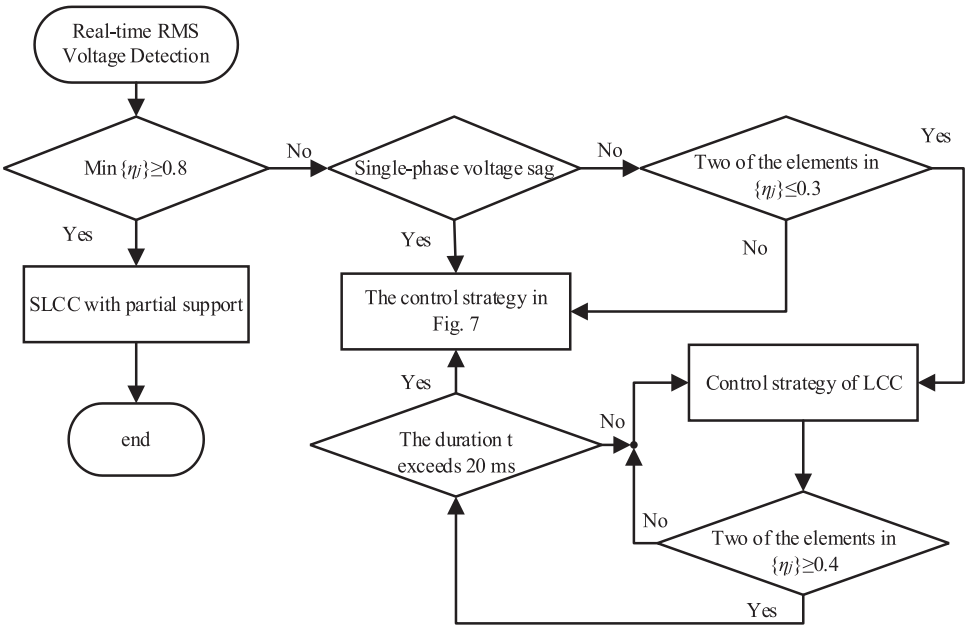

Figure 8: The transition conditions among different operating modes

4 Analysis of Simulation Results

To validate the effectiveness of the proposed coordinated control strategy, a simulation model is built in PLECS based on the second phase of the Yangzhou–Zhenjiang HVDC transmission project. The model topology is consistent with Fig. 1 when the number of series-connected six-pulse converter valves is unitary, with the SVF installed on the inverter side. The overall simulation structure diagram used in this paper is shown in Fig. 9. The SLCC system parameters are the same as those in Table 1.

4.1 Simulation Analysis of SLCC System without Considering SVF Withstand Capability

The steady-state operation results of the SLCC system are shown in Fig. 10.

As shown in Fig. 10, the DC-side voltage of the established SLCC system model is 200 kV and the DC current is 3 kA in steady state, consistent with the set values. The active power transmission is 600 MW in steady state, matching the required value, and the reactive power transmission remains stable at approximately 0 MW, meeting the operational requirements of the SLCC system under steady state.

To compare the impact of considering the SVF withstand capability on the SLCC coordinated control strategy, the SVF blocking function is initially disabled, i.e., the SVF withstand capability is set to infinite. Under this condition, the SLCC system is controlled using both the strategy without considering the SVF withstand capability [14] and the one considering it, observing its operation under different fault conditions. The simulation sets three AC grid fault conditions in total:

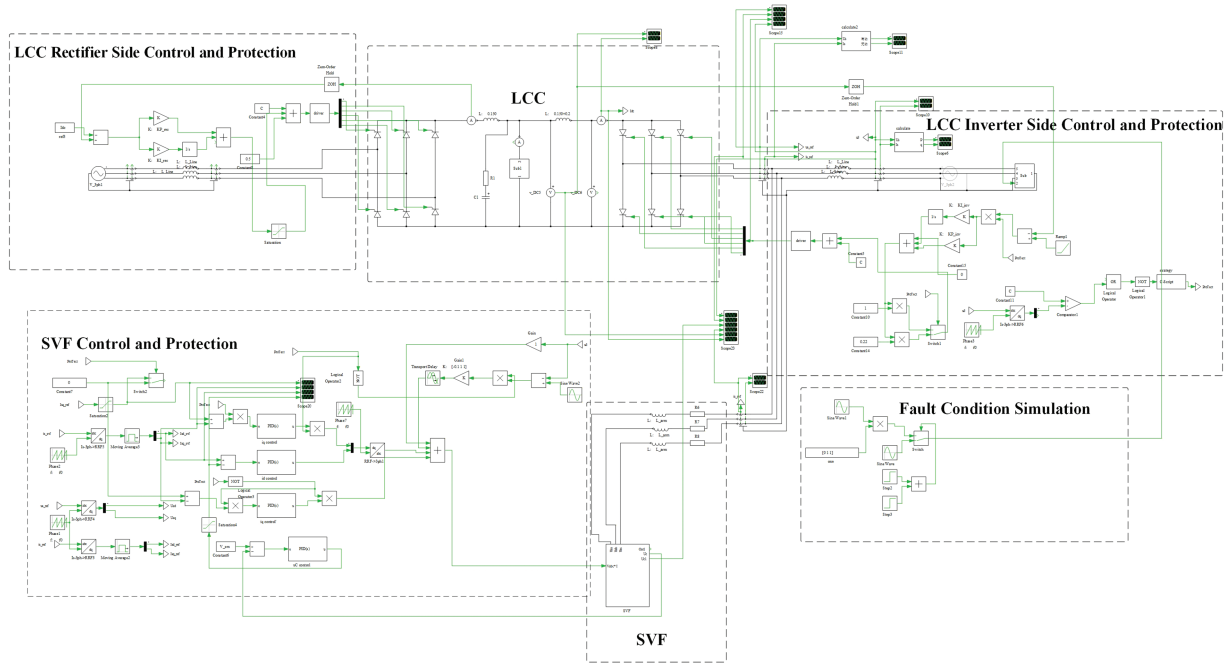

Figure 9: Overall simulation structure diagram used in this paper

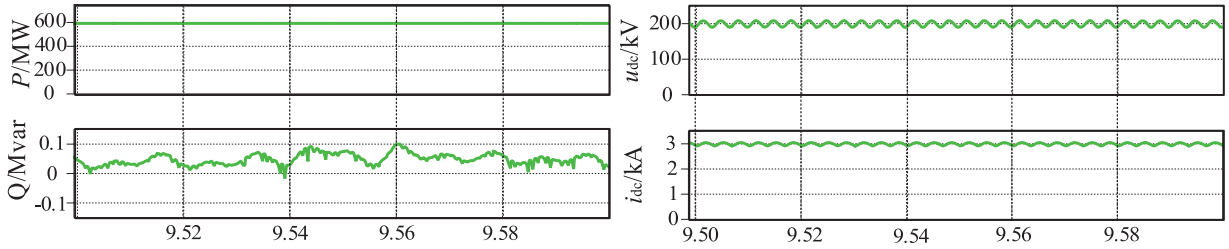

Figure 10: SLCC steady-state operation results

Fault condition 1: The three-phase voltages of the receiving-end grid sag to 0.6 p.u., and the converter station firing angle decreases to 60% of its steady-state value.

Fault condition 2: A single-phase voltage of the receiving-end grid sags to 0.6 p.u., and the converter station firing angle decreases to 75% of its steady-state value.

Fault condition 3: A single-phase ground fault occurs in the receiving-end grid, and the converter station firing angle decreases to 22% of its steady-state value.

(All faults occur at t = 10 s.)

As shown in Fig. 11, the control strategy without considering the SVF withstand capability accelerates the commutation process through SVF compensation voltage. This acceleration reduces the risk of commutation failure. In fault condition 2, where the voltage sag is not severe, normal operation is maintained. This performance appears to demonstrate the SVF's ability to suppress commutation failure under fault conditions.

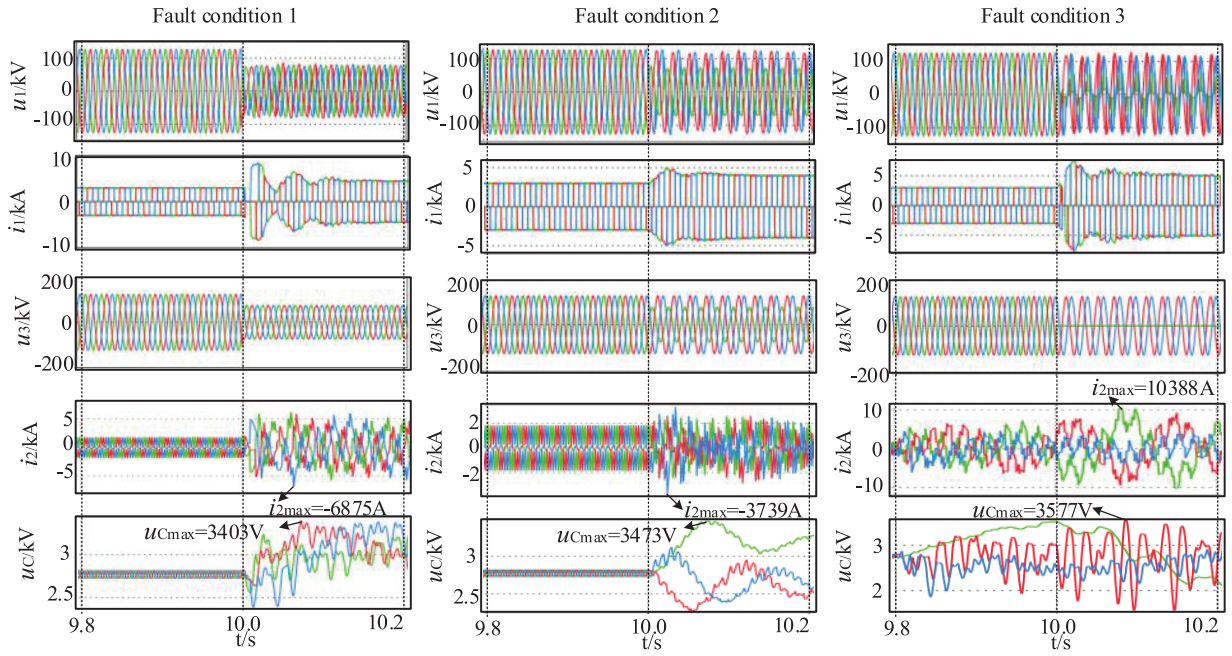

Figure 11: SLCC operation under different fault conditions with the control strategy without considering SVF withstand capability

However, when fault severity increases, the coordination between the SVF and LCC control strategies becomes poor. This poor coordination results from the lack of precise consideration of the SVF's withstand capability. Consequently, excessive inrush current occurs in the SVF bridge arms during faults. The instantaneous maximum current reaches 6875 A in fault condition 1 and 10,388 A in fault condition 3. Both values exceed the maximum current stress that the IGBTs can withstand.

Furthermore, in fault condition 3, the maximum submodule capacitor voltage reaches 3577 V, exceeding its allowable range. This means that in practice, the SVF would block under these fault conditions. Such blocking would cause the converter station to lose voltage support from the SVF. As a result, the SLCC system's ability to support safe commutation would degrade to a level comparable to an LCC system. This degradation would cause the complete loss of the enhanced commutation failure suppression capability provided by the SLCC.

4.2 Simulation Case of SLCC System Considering SVF Withstand Capability

As shown in Fig. 12, the proposed control strategy fully accounts for the SVF withstand capability. It applies the voltage feedforward increment within safe operational boundaries during faults. This approach enables the SVF to quickly transition to stable voltage support under system fault conditions. At the same time, it prevents bridge arm current overload that would result from excessive SVF voltage.

In fault condition 1, the maximum instantaneous SVF bridge arm current reaches 4235 A, while the maximum submodule capacitor voltage is 3100 V. In fault condition 3, the corresponding values are 4233 A and 3149 V, respectively. Under both fault scenarios, commutation failure is successfully avoided, and the SVF voltage and current remain within allowable limits.

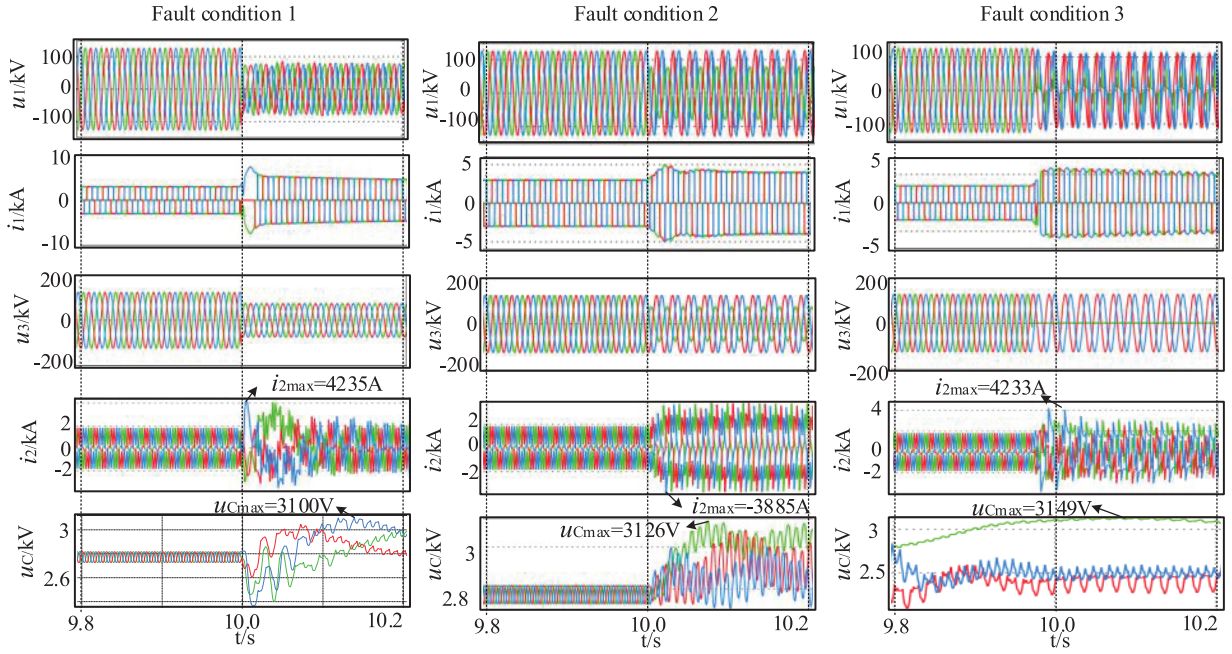

Figure 12: System operation under different fault conditions with the control strategy considering SVF withstand capability

A comparison with the results in Fig. 11 clearly shows that the proposed control method enables fault ride-through of the SLCC system without triggering SVF blocking. Moreover, it significantly reduces the demand on the SVF withstand capability. Specifically, the required SVF bridge arm current withstand capability is reduced by 38.4% in fault condition 1 and by 59.2% in fault condition 3.

As indicated in Table 4, the more severe the fault condition, the more significant the reduction in SVF overvoltage and overcurrent achieved by the proposed control strategy compared to the strategy that does not consider the SVF withstand capability. This is because the proposed control strategy fully leverages the voltage support capability of the SVF, thereby substantially reducing the redundancy requirements for the SVF's withstand capability.

Table 4: Comparison of results under different fault conditions

Fault condition	$\lvert i_{2j} \rvert$	u_{Cmax}	Commutation status	SVF blocking status
Three-phase voltage sags to 0.7 p.u. firing angle reduced to 80% without considering withstand capability	3860 A	3158 V	No failure	No blocking
Three-phase voltage sags to 0.4 p.u. firing angle reduced to 40% without considering withstand capability	10,525 A	3466 V	Failure	Blocking
Three-phase voltage sags to 0.4 p.u. firing angle reduced to 40% considering withstand capability	4646 A	3213 V	No failure	No blocking

(Continued)

Table 4 (continued)

Fault condition	$\lvert i_{2j} \rvert$	u_{Cmax}	Commutation status	SVF blocking status
Three-phase voltage sags to 0.5 p.u. firing angle reduced to 70% without considering withstand capability	3990 A	3347 V	No failure	No blocking
Three-phase voltage sags to 0.4 p.u. firing angle reduced to 55% without considering withstand capability	7802 A	4305 V	No failure	Blocking
Three-phase voltage sags to 0.4 p.u. firing angle reduced to 55% considering withstand capability	4632 A	3420 V	No failure	No blocking

To validate the robustness of the proposed strategy with respect to variations in I_{permit}, a grid voltage sag of 0.4 p.u. is applied, and I_{permit} is reduced to 90% of its nominal value (i.e., 4230 A). The corresponding system response is shown in Fig. 13a. For comparison, Fig. 13b presents the response when I_{permit} remains at its nominal value of 4700 A.

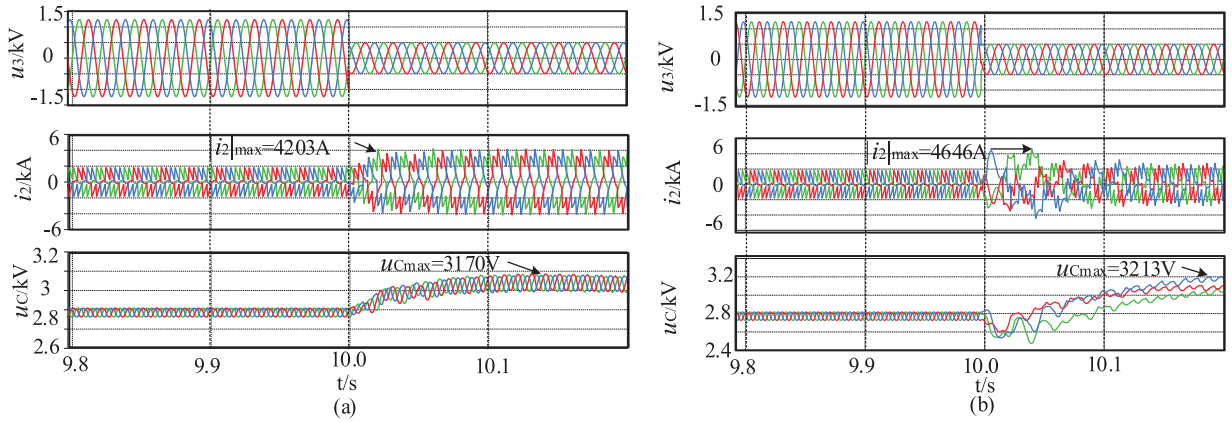

Figure 13: Comparison of SVF performance under different I_{permit} settings

As shown in Fig. 13a, even when the grid voltage drops to 0.4 p.u., the control strategy proposed in this paper can still adaptively limit the bridge-arm current of the SVF within the allowable range defined by I_{permit}. This is because reducing the setting of I_{permit} effectively weakens the dynamic support capability of the SVF. Under the proposed control strategy, the system automatically adjusts the operational boundaries of the SVF according to the updated I_{permit} value and correspondingly modifies its feedforward gain Kv. The reduction in SVF output caused by the lower I_{permit}—and its adverse impact on the commutation process—is compensated by adjusting the inverter extinction angle β.

However, this compensation comes at the cost of reduced power transmission. In the scenario shown in Fig. 13a, the firing angle of the inverter station has been reduced to 20% to ensure commutation security, whereas in Fig. 13b, 13a reduction to only 40% is sufficient. Therefore, in practical applications, the margin

of I_{permit} should not be set too conservatively. An appropriate level of headroom must be retained to balance both fault support capability and power transfer efficiency.

4.3 Simulation Results of SLCC under Different Control Strategies

To intuitively demonstrate the advantages of the SLCC feedforward coordinated control strategy based on angle limiting over conventional methods during voltage sag faults at the receiving-end grid, this paper establishes Fault Condition 4: a single-phase voltage sag to 0.4 p.u. at the receiving-end grid, and the converter station firing angle decreases to 55% of its steady-state value. With the SVF blocking function enabled, the SLCC system is controlled using both direct voltage feedforward control [14] and the strategy proposed in this paper, yielding the results presented in Fig. 14.

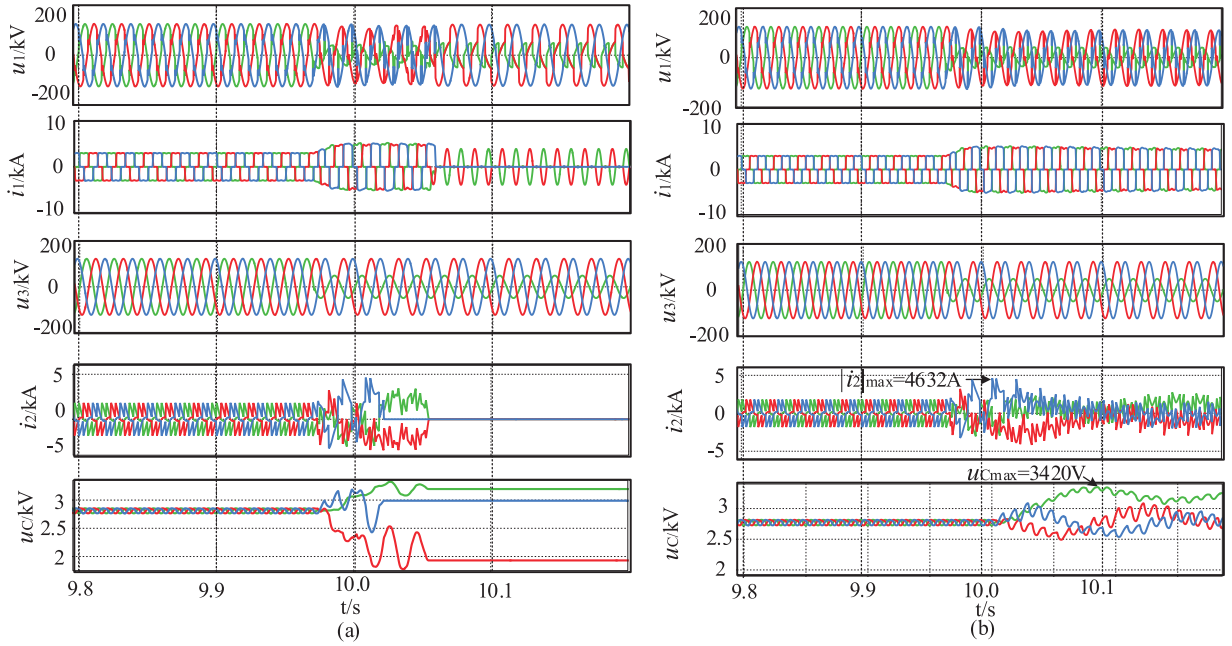

Figure 14: Comparison of operation of the SLCC system under fault condition 4 (a single-phase voltages of the receiving-end grid sag to 0.4 p.u.) with different control strategies

Fig. 14a presents the results using direct feedforward control, while Fig. 14b shows the results using the proposed strategy. In fact, the direct feedforward control results are obtained based on the control strategy without considering withstand capability discussed in Section 4.1, but with the blocking effects caused by SVF withstand capability limits taken into account. As shown in Fig. 14, when a single-phase voltage sag of 0.4 p.u. occurs in the receiving-end grid of the SLCC system, the direct feedforward control causes SVF blocking due to excessive regulation of the SVF, leading to degradation of the SLCC system into an LCC system and resulting in commutation failure. In contrast, with the proposed strategy, the SLCC system can still maintain continuous operation.

To verify the improvement effect of the method proposed in this paper compared to traditional approaches when the fault condition further intensifies, this paper sets Fault Condition 5: the three-phase voltages of the receiving-end grid sag to 0.4 p.u., and the converter station firing angle decreases to 40% of its steady-state value.

Under this condition, the SLCC system is controlled using the constant voltage control with current limiter and the strategy proposed in this paper, respectively. The results are shown in Fig. 15.

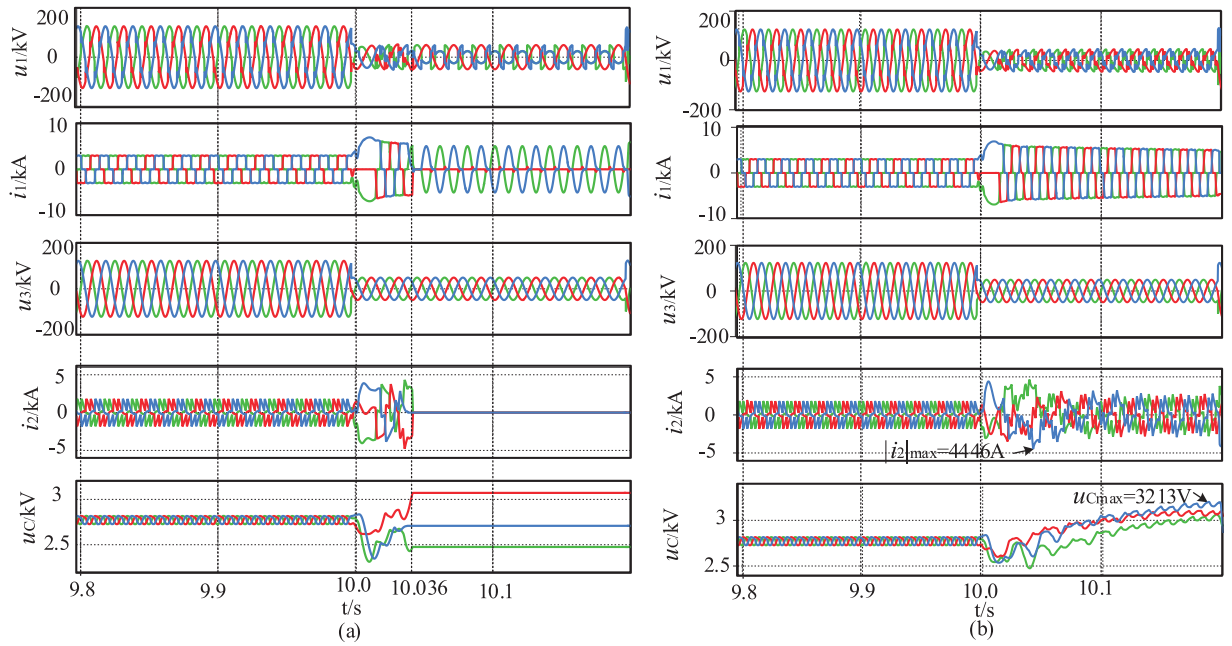

Figure 15: Comparison of operation of the SLCC system under fault condition 5 with different control strategies

Fig. 15a shows the results obtained using the constant voltage control with current limiter, while Fig. 15b presents the results from the strategy proposed in this paper. As shown in Fig. 15, when the voltage sag at the receiving-end grid of the SLCC system further intensifies, the SVF employing the constant voltage control with current limiter already experiences an overcurrent issue in its bridge arm current i_2, leading to SVF blocking. Consequently, the SLCC system degenerates into an LCC system, resulting in commutation failure. In contrast, under the same operating condition, the strategy proposed herein maintains the maximum SVF bridge arm current at 4446 A and the maximum submodule capacitor voltage at 3240 V. This means it successfully keeps both the SVF bridge arm current and the submodule capacitor voltage within their allowable limits, prevents commutation failure in the SLCC system, and ensures its continued operation.

To clearly demonstrate the advantages of the strategy proposed in this paper over other strategies under AC system voltage sag fault conditions, the blocking boundaries of SVF for various strategies are summarized in Table 5.

As can be seen from Table 5, when a voltage sag occurs in the receiving-end grid—whether it is a single-phase or three-phase fault—compared to the feedforward control strategy that does not consider withstand capability or the constant voltage control method with a current limiter, the strategy proposed in this paper can ensure non-blocking operation of the SVF and maintain safe commutation of the SLCC under relatively more severe fault conditions. The reason is that, under fault conditions, compared to other control strategies, the proposed control strategy enhances the voltage support capability of the SVF by accounting for its withstand capability. This reduces the required adjustment of the converter station's control angle, thereby enabling safe commutation under more severe voltage sag faults.

Table 5: Comparison of SVF blocking under different strategies

Fault condition	Strategies	SVF blocking boundary
Single-phase voltage sag	Feedforward control method without considering withstand capability [14]	Voltage sags to 0.4 p.u.
	Constant voltage control with current limiter [15]	Voltage sags to 0.6 p.u.
	The strategy proposed in this paper	No blocking
Three-phase voltage sag	Feedforward control method without considering withstand capability [1]	Voltage sags to 0.6 p.u.
	Constant voltage control with current limiter [15]	Voltage sags to 0.6 p.u.
	The strategy proposed in this paper	Voltage sags to 0.3 p.u.

5 Conclusion

To fully leverage the flexible regulation capability of the SVF for voltage support in the SLCC system under fault conditions, this paper, focusing on AC grid faults and based on the analysis of the SVF withstand capability combined with the traditional LCC control strategy under fault conditions, proposes a coordinated control strategy for the SLCC system that considers the SVF withstand capability. Through theoretical analysis and simulation verification, the following conclusions are drawn:

(1) Under fault conditions, the current in the SLCC increases abnormally and causes an increase in the SVF bridge arm current through the coupling point, leading to the SVF bridge arm current exceeding its limit and resulting in SVF overcurrent blocking. Taking the simulation example of the Yangzhou-Zhenjiang HVDC transmission project phase II as an example, if the SVF voltage is not limited, the SVF bridge arm current can reach 10 kA under fault conditions. If voltage support from the SVF is still expected, it would inevitably impose higher demands on the SVF's current withstand capability.

(2) Under fault conditions, the voltage support provided by the SVF to the SLCC also leads to abnormal fluctuations in the SVF submodule capacitor voltage, causing the SVF submodule capacitor voltage to exceed its limit and resulting in SVF overvoltage blocking. Simultaneously, as the DC current increases, the influence of the SVF voltage command value on the SVF submodule capacitor voltage intensifies. When the AC grid voltage sags significantly, the amplitude of the SVF submodule capacitor voltage increment can reach 1000 V, causing the SVF to block due to exceeding its voltage withstand capability.

(3) The proposed coordinated control strategy, based on the quantitative analysis of the SVF withstand capability, introduces a feedforward control strategy incorporating angle limiting, which effectively reduces the current and voltage impact on the SVF and prevents SVF blocking. Particularly in the most common single-phase ground fault on the AC side, the proposed strategy reduces the demand on the SVF bridge arm current withstand capability by 59.2%, balancing the SVF voltage support regulation speed with SVF non-blocking operation. Thereby, it ensures the continuous operation of the SVF under fault conditions and maintains the safe commutation capability of the SLCC.

Acknowledgement: The authors are thankful to the facility provided by the State Grid Jiangsu Electric Power Company Construction Branch for conducting this research.

Funding Statement: The authors received funding from the Science and Technology Project of State Grid Jiangsu Electric Power Co., Ltd. (Grant No. J2024201) for this study.

Author Contributions: The authors confirm contribution to the paper as follows: Overall research topic and supervision: Xintong Mao, Yechi Xu; Tables and figures adjustments: Zhihan Liu, Yumeng Wang; Draft manuscript writing: Yaowen Sun, Chuyang Wang. All authors reviewed and approved the final version of the manuscript.

Availability of Data and Materials: The authors ensure the authenticity and validity of the materials and data in the paper.

Ethics Approval: Not applicable.

Conflicts of Interest: The authors declare no conflicts of interest.

Appendix A

Table A1: The meaning of each variable

Variable name	Meaning
u_{dc}	DC-side voltage
u_{dc}^{*}	DC-side voltage command value
V_{dc}	DC-side voltage rated value
i_{dc}	DC-side current
L_1	DC-side inductance
L_2	SVF inductance
L_3	Grid-side equivalent inductance
u_1	Converter valve bus voltage
u_{1j}	Converter valve j-phase bus voltage
U_2	Amplitude of the SVF three-phase cascaded bridge voltage
U_2^{*}	SVF three-phase cascaded bridge voltage amplitude command value
u_2	SVF three-phase cascaded bridge voltage
u_2^{*}	SVF three-phase cascaded bridge voltage command value
u_{2j}	SVF j-phase cascaded bridge voltage
U_3	Amplitude of the grid three-phase voltage
u_3	Grid three-phase voltage
u_{3j}	Grid j-phase voltage
u_{3j}^{*}	Grid j-phase voltage command value
i_2	SVF three-phase bridge arm current
i_{1j}	Converter valve j-phase line current
i_{2j}	SVF j-phase line current
i_{3j}	Grid j-phase line current
ω_0	Grid voltage angular frequency
η_j	Voltage sag severity of the j-phase in the receiving-end AC system
P	System active power transmission
P^{*}	System active power command value
Q	System reactive power transmission
Q^{*}	System reactive power command value
I_{permit}	Peak current boundary value triggering IGBT blocking in the SVF submodule
I_{CRM}	IGBT's maximum repetitive peak collector current
u_{C}	Submodule capacitor voltage value

(Continued)

Table A1 (continued)

Variable name	Meaning
V_{C}	Submodule capacitor rated voltage
Δu_{C}	SVF submodule capacitor voltage increment
C_{f}	Capacitance of a single SVF submodule
Ξ	Maximum allowable increase rate of submodule capacitor voltage
i_{d}	Active current
i_{d}^{*}	Active current command value
i_{q}	Reactive current
i_{q}^{*}	Reactive current command value
$i_{1\mathrm{d}}$	Active component of converter valve line current
u_{1}^{*}	Converter valve bus voltage command value
$i_{1\mathrm{q}}$	Reactive component of converter valve line current
$i_{2\mathrm{d}}$	Active component in SVF line current
$i_{2\mathrm{q}}$	Reactive component in SVF line current
α	Firing angle
β	Inversion angle
$\beta_{\min}$	Minimum inversion angle
γ	Extinction angle
M	overlap angle
θ	Margin angle
$\theta_{\min}$	Minimum margin angle
u_{gn}	Gate signal of the n-th thyristor
S_{jn}	Switching signal of the n-th submodule in the j-phase bridge arm of the SVF
SM_{jn}	The n-th submodule in the j-phase bridge arm of the SVF
$i_{\mathrm{F}h}$	h-th characteristic harmonic current of the SVF
$i_{\mathrm{L}h}$	h-th characteristic harmonic current of the LCC
V_{m1}	Maximum voltage command value of SVF three-phase cascaded bridge under current withstand capability boundary condition
V_{m2}	Maximum voltage command value of SVF three-phase cascaded bridge under voltage withstand capability boundary condition
K_{v}	Voltage feedforward coefficient
ΔU_2	Amplitude of submodule capacitor voltage
φ_{i1j}	Phase angle of converter valve j-phase line current
$\varphi_{\mathrm{u}2j}$	Phase angle of SVF j-phase cascaded bridge voltage
$\varphi_{\mathrm{u}2j}^{*}$	Phase angle command value of SVF j-phase cascaded bridge voltage
$\varphi_{\mathrm{u}3j}$	Phase angle of grid j-phase phase voltage
φ_{uc}	Phase angle of SVF submodule capacitor voltage
N_{sub}	Number of submodules put into operation in a single-phase bridge arm
N	Number of series-connected six-pulse converter valves in a single converter station

Appendix B

Appendix B.1 The Detailed Derivation of Eq. (7)

$$\begin{aligned} i_{2j} &= \frac{1}{L_2+L_3}\int\left[\eta_j U_3\sin(\omega_0 t)-\left(1+\frac{N_{\text{sub}}\Delta u_c}{u_{\text{dc}}}\right)U_2\sin\left(\omega_0 t+\varphi_{\text{u2}j}\right)\right]dt+\frac{L_3}{L_2+L_3}i_{\text{dc}} \\ &= -\frac{1}{\omega_0(L_2+L_3)}\eta_j U_3\cos(\omega_0 t)+\frac{1}{\omega_0(L_2+L_3)}\left(1+\frac{N_{\text{sub}}\Delta u_c}{u_{\text{dc}}}\right)U_2\cos\left(\omega_0 t+\varphi_{\text{u2}j}\right)+\frac{L_3}{L_2+L_3}i_{\text{dc}} \\ &= -\frac{1}{\omega_0(L_2+L_3)}\eta_j U_3\cos(\omega_0 t)+\frac{1}{\omega_0(L_2+L_3)}U_2\cos\left(\omega_0 t+\varphi_{\text{u2}j}\right) \\ &\quad+\frac{1}{\omega_0(L_2+L_3)}\frac{N_{\text{sub}}\Delta u_c}{u_{\text{dc}}}U_2\cos\left(\omega_0 t+\varphi_{\text{u2}j}\right)+\frac{L_3}{L_2+L_3}i_{\text{dc}} \end{aligned} \tag{A1}$$

Assuming Eq. (A2),

$$\Delta u_c = \Delta U_2\sin(\omega_0 t+\varphi_{\text{uc}}) \tag{A2}$$

Substituting it into Eq. (A1) yields:

$$\begin{aligned} i_{2j} &= -\frac{1}{\omega_0(L_2+L_3)}\eta_j U_3\cos(\omega_0 t)+\frac{1}{\omega_0(L_2+L_3)}U_2\cos\left(\omega_0 t+\varphi_{\text{u2}j}\right) \\ &\quad+\frac{1}{\omega_0(L_2+L_3)}\frac{N_{\text{sub}}\Delta U_2\sin(\omega_0 t+\varphi_{\text{uc}})}{u_{\text{dc}}}U_2\cos\left(\omega_0 t+\varphi_{\text{u2}j}\right)+\frac{L_3}{L_2+L_3}i_{\text{dc}} \\ &= -\frac{1}{\omega_0(L_2+L_3)}\eta_j U_3\cos(\omega_0 t)+\frac{1}{\omega_0(L_2+L_3)}U_2\cos\left(\omega_0 t+\varphi_{\text{u2}j}\right)+\frac{L_3}{L_2+L_3}i_{\text{dc}} \\ &\quad+\frac{1}{2\omega_0(L_2+L_3)}\frac{N_{\text{sub}}\Delta U_2 U_2}{u_{\text{dc}}}\left[\sin\left(2\omega_0 t+\varphi_{\text{uc}}+\varphi_{\text{u2}j}\right)+\sin\left(\varphi_{\text{uc}}-\varphi_{\text{u2}j}\right)\right] \end{aligned} \tag{A3}$$

Since φ_{uc} is phase angle of SVF submodule capacitor voltage, thus

$$\varphi_{\text{uc}} = -\frac{\pi}{2} \tag{A4}$$

Substituting it into Eq. (A3) yields Eq. (A5).

$$\begin{aligned} i_{2j} &= -\frac{1}{\omega_0(L_2+L_3)}\eta_j U_3\cos(\omega_0 t)+\frac{1}{\omega_0(L_2+L_3)}U_2\cos\left(\omega_0 t+\varphi_{\text{u2}j}\right)+\frac{L_3}{L_2+L_3}i_{\text{dc}} \\ &\quad+\frac{1}{2\omega_0(L_2+L_3)}\frac{N_{\text{sub}}\Delta U_2 U_2}{u_{\text{dc}}}\left[\sin\left(2\omega_0 t-\frac{\pi}{2}+\varphi_{\text{u2}j}\right)+\sin\left(-\frac{\pi}{2}-\varphi_{\text{u2}j}\right)\right] \\ &= -\frac{1}{\omega_0(L_2+L_3)}\eta_j U_3\cos(\omega_0 t)+\frac{1}{\omega_0(L_2+L_3)}U_2\cos\left(\omega_0 t+\varphi_{\text{u2}j}\right)+\frac{L_3}{L_2+L_3}i_{\text{dc}} \\ &\quad+\frac{1}{2\omega_0(L_2+L_3)}\frac{N_{\text{sub}}\Delta U_2 U_2}{u_{\text{dc}}}\left[-\cos\left(2\omega_0 t+\varphi_{\text{u2}j}\right)-\cos\left(\varphi_{\text{u2}j}\right)\right] \\ &= -\frac{1}{\omega_0(L_2+L_3)}\eta_j U_3\cos(\omega_0 t)+\frac{1}{\omega_0(L_2+L_3)}U_2\cos\left(\omega_0 t+\varphi_{\text{u2}j}\right)+\frac{L_3}{L_2+L_3}i_{\text{dc}} \\ &\quad-\frac{1}{2\omega_0(L_2+L_3)}\frac{N_{\text{sub}}\Delta U_2 U_2}{u_{\text{dc}}}\cos\left(2\omega_0 t+\varphi_{\text{u2}j}\right)-\frac{1}{2\omega_0(L_2+L_3)}\frac{N_{\text{sub}}\Delta U_2 U_2}{u_{\text{dc}}}\cos\left(\varphi_{\text{u2}j}\right) \end{aligned}$$

$$= \left[-\frac{1}{\omega_0 (L_2 + L_3)} \eta_j U_3 + \frac{1}{\omega_0 (L_2 + L_3)} U_2 \cos\left(\varphi_{u2j}\right) \right] \cos(\omega_0 t) - \frac{1}{\omega_0 (L_2 + L_3)} U_2 \sin\left(\varphi_{u2j}\right) \sin(\omega_0 t)$$
$$- \frac{1}{2\omega_0 (L_2 + L_3)} \frac{N_{sub} \Delta U_2 U_2}{u_{dc}} \cos\left(2\omega_0 t + \varphi_{u2j}\right) + \frac{L_3}{L_2 + L_3} i_{dc} - \frac{1}{2\omega_0 (L_2 + L_3)} \frac{N_{sub} \Delta U_2 U_2}{u_{dc}} \cos\left(\varphi_{u2j}\right) \tag{A5}$$

Further, yields Eq. (A6):

$$i_{2j} = \sqrt{\left[-\frac{1}{\omega_0 (L_2 + L_3)} \eta_j U_3 + \frac{1}{\omega_0 (L_2 + L_3)} U_2 \cos\left(\varphi_{u2j}\right) \right]^2 + \left[\frac{1}{\omega_0 (L_2 + L_3)} U_2 \sin\left(\varphi_{u2j}\right) \right]^2} \sin(\omega_0 t + \varphi)$$
$$- \frac{1}{2\omega_0 (L_2 + L_3)} \frac{N_{sub} \Delta U_2 U_2}{u_{dc}} \cos\left(2\omega_0 t + \varphi_{u2j}\right) + \frac{L_3}{L_2 + L_3} i_{dc} - \frac{1}{2\omega_0 (L_2 + L_3)} \frac{N_{sub} \Delta U_2 U_2}{u_{dc}} \cos\left(\varphi_{u2j}\right) \tag{A6}$$

where,

$$\begin{cases} \cos\varphi = \dfrac{-\frac{1}{\omega_0 (L_2 + L_3)} U_2 \sin\left(\varphi_{u2j}\right)}{\sqrt{\left[-\frac{1}{\omega_0 (L_2 + L_3)} \eta_j U_3 + \frac{1}{\omega_0 (L_2 + L_3)} U_2 \cos\left(\varphi_{u2j}\right) \right]^2 + \left[\frac{1}{\omega_0 (L_2 + L_3)} U_2 \sin\left(\varphi_{u2j}\right) \right]^2}} \\ \sin\varphi = \dfrac{-\frac{1}{\omega_0 (L_2 + L_3)} \eta_j U_3 + \frac{1}{\omega_0 (L_2 + L_3)} U_2 \cos\left(\varphi_{u2j}\right)}{\sqrt{\left[-\frac{1}{\omega_0 (L_2 + L_3)} \eta_j U_3 + \frac{1}{\omega_0 (L_2 + L_3)} U_2 \cos\left(\varphi_{u2j}\right) \right]^2 + \left[\frac{1}{\omega_0 (L_2 + L_3)} U_2 \sin\left(\varphi_{u2j}\right) \right]^2}} \end{cases} \tag{A7}$$

In fact, since

$$\frac{1}{2\omega_0 (L_2 + L_3)} \frac{N_{sub} \Delta U_2 U_2}{u_{dc}} < 0.01 \frac{L_3}{L_2 + L_3} i_{dc} \tag{A8}$$

Thus,

$$i_{2j} \approx \sqrt{\left[\begin{matrix} -\frac{1}{\omega_0 (L_2 + L_3)} \eta_j U_3 \\ + \frac{1}{\omega_0 (L_2 + L_3)} U_2 \cos\left(\varphi_{u2j}\right) \end{matrix} \right]^2 + \left[\frac{1}{\omega_0 (L_2 + L_3)} U_2 \sin\left(\varphi_{u2j}\right) \right]^2} \sin(\omega_0 t + \varphi) + \frac{L_3}{L_2 + L_3} i_{dc} \tag{A9}$$

Appendix B.2 The Detailed Derivation of Eq. (11)

Substituting Eq. (7) into (9) yields:

$$\Delta u_C = \frac{1}{C_f} \int i_C dt$$
$$= \frac{1}{N_{sub} C_f} \int \frac{u_{2j}}{u_C} \cdot \left[\sqrt{\left[\begin{matrix} -\frac{1}{\omega_0 (L_2 + L_3)} \eta_j U_3 \\ + \frac{1}{\omega_0 (L_2 + L_3)} U_2 \cos\left(\varphi_{u2j}\right) \end{matrix} \right]^2 + \left[\frac{1}{\omega_0 (L_2 + L_3)} U_2 \sin\left(\varphi_{u2j}\right) \right]^2} \sin(\omega_0 t + \varphi) + \frac{L_3}{L_2 + L_3} i_{dc} \right] dt \tag{A10}$$

In fact, according to the derivation in Appendix A, the impact of ΔU_2 is negligible; thus, it can be assumed as Eq. (A11).

$$\begin{aligned} u_{2j} &= \left(1+\frac{N_{\text{sub}}\Delta u_{\text{c}}}{u_{\text{dc}}}\right)U_2\sin\left(\omega_0 t+\varphi_{\text{u}2j}\right) \\ &= \left(1+\frac{N_{\text{sub}}\Delta U_2\sin\left(\omega_0 t+\varphi_{\text{uc}}\right)}{u_{\text{dc}}}\right)U_2\sin\left(\omega_0 t+\varphi_{\text{u}2j}\right) \\ &\approx U_2\sin\left(\omega_0 t+\varphi_{\text{u}2j}\right) \end{aligned} \tag{A11}$$

Substituting Eq. (A11) into (A10) yields:

$$\begin{aligned} \Delta u_{\text{C}} &\approx \frac{1}{N_{\text{sub}}C_{\text{f}}}\int\frac{U_2\sin\left(\omega_0 t+\varphi_{\text{u}2j}\right)}{u_{\text{C}}}\cdot\left[\sqrt{\begin{bmatrix}-\dfrac{1}{\omega_0\left(L_2+L_3\right)}\eta_j U_3 \\ +\dfrac{1}{\omega_0\left(L_2+L_3\right)}U_2\cos\left(\varphi_{\text{u}2j}\right)\end{bmatrix}^2+\left[\frac{1}{\omega_0\left(L_2+L_3\right)}U_2\sin\left(\varphi_{\text{u}2j}\right)\right]^2}\sin\left(\omega_0 t+\varphi\right)+\frac{L_3}{L_2+L_3}i_{\text{dc}}\right]dt \\ &= \frac{U_2}{N_{\text{sub}}C_{\text{f}}u_{\text{C}}}\int\left\{\sqrt{\begin{bmatrix}-\dfrac{1}{\omega_0\left(L_2+L_3\right)}\eta_j U_3 \\ +\dfrac{1}{\omega_0\left(L_2+L_3\right)}U_2\cos\left(\varphi_{\text{u}2j}\right)\end{bmatrix}^2+\left[\frac{1}{\omega_0\left(L_2+L_3\right)}U_2\sin\left(\varphi_{\text{u}2j}\right)\right]^2}\frac{\cos\left(\varphi_{\text{u}2j}-\varphi\right)-\cos\left(2\omega_0 t+\varphi_{\text{u}2j}+\varphi\right)}{2}+\frac{L_3}{L_2+L_3}i_{\text{dc}}\sin\left(\omega_0 t+\varphi_{\text{u}2j}\right)\right\}dt \end{aligned} \tag{A12}$$

Since

$$\begin{aligned} B &= \frac{1}{2}\sqrt{\left[-\frac{1}{\omega_0\left(L_2+L_3\right)}\eta_j U_3+\frac{1}{\omega_0\left(L_2+L_3\right)}U_2\cos\left(\varphi_{\text{u}2j}\right)\right]^2+\left[\frac{1}{\omega_0\left(L_2+L_3\right)}U_2\sin\left(\varphi_{\text{u}2j}\right)\right]^2} \\ &<< \frac{L_3}{L_2+L_3}i_{\text{dc}} \end{aligned} \tag{A13}$$

Thus,

$$\begin{aligned} \Delta u_{\text{C}} &= \frac{U_2}{N_{\text{sub}}C_{\text{f}}u_{\text{C}}}\int\left\{B\cos\left(\varphi_{\text{u}2j}-\varphi\right)-B\cos\left(2\omega_0 t+\varphi_{\text{u}2j}+\varphi\right)+\frac{L_3}{L_2+L_3}i_{\text{dc}}\sin\left(\omega_0 t+\varphi_{\text{u}2j}\right)\right\}dt \\ &\approx \frac{-1}{N_{\text{sub}}C_{\text{f}}}\frac{U_2 L_3}{\left(L_2+L_3\right)u_{\text{C}}\omega_0}\cos\left(\omega_0 t+\varphi_{\text{u}2j}\right)i_{\text{dc}} \end{aligned} \tag{A14}$$

Appendix B.3 The Detailed Derivation of Eq. (15)

The full derivation of Eq. (15) is as follow:

First, according to Fig. 5, the following relationship exists (j = a, b, c):

$$\begin{cases} i_{1j}+i_{2j}=i_{3j} \\ i_{\text{dc}}=i_{1\text{a}}+i_{1\text{b}} \end{cases} \tag{A15}$$

$$\begin{cases} u_{\mathrm{a}} - L_2 \dfrac{di_{2\mathrm{a}}}{dt} - L_3 \dfrac{d\left(i_{1\mathrm{a}} + i_{2\mathrm{a}}\right)}{dt} - u_{\mathrm{sa}} = 0 \\ u_{\mathrm{b}} - L_2 \dfrac{di_{2\mathrm{b}}}{dt} - L_3 \dfrac{d\left(i_{1\mathrm{b}} + i_{2\mathrm{b}}\right)}{dt} - u_{\mathrm{sb}} = 0 \end{cases} \tag{A16}$$

$$u_{3j} = u_{2j} - L\frac{di_{2j}}{dt} = u_{1j} - L\frac{di_{1j}}{dt} \tag{A17}$$

Furthermore, based on the nature of the commutation process, the following relationship exists (with the natural commutation point at $\pi/6$):

$$i_{\mathrm{dc}} = \int_{\alpha-\frac{\pi}{6}}^{\alpha-\frac{\pi}{6}+\mu} \left(\frac{di_{1\mathrm{a}}}{dt} - \frac{di_{1\mathrm{b}}}{dt}\right) dt \tag{A18}$$

From Eq. (A17), (A20) is obtained:

$$\begin{cases} \dfrac{di_{1\mathrm{a}}}{dt} = \dfrac{1}{L_3}\left(u_{2\mathrm{a}} - u_{3\mathrm{a}}\right) - \dfrac{L_2 + L_3}{L_2}\dfrac{di_{2\mathrm{a}}}{dt} \\ \dfrac{di_{1\mathrm{b}}}{dt} = \dfrac{1}{L_3}\left(u_{2\mathrm{b}} - u_{3\mathrm{b}}\right) - \dfrac{L_2 + L_3}{L_2}\dfrac{di_{2\mathrm{b}}}{dt} \end{cases} \tag{A19}$$

From Eq. (A20), (A21) is obtained:

$$\frac{di_{1\mathrm{a}}}{dt} - \frac{di_{1\mathrm{b}}}{dt} = \left[\frac{1}{L_2}\left(u_{2\mathrm{a}} - u_{2\mathrm{b}}\right) + \frac{1}{L_3}\left(u_{3\mathrm{a}} - u_{3\mathrm{b}}\right)\right] \tag{A20}$$

Substituting Eq. (A21) into (A19) yields Eq. (14)

Applying a first-order Taylor approximation to Eq. (14) yields Eq. (A21).

$$i_{\mathrm{dc}} = \frac{\sqrt{3}}{2\omega_0}\left[\frac{U_3}{L_3}\left(\cos\left(\alpha\right) - \cos\left(\alpha+\mu\right)\right) + \frac{U_2}{L_2}\left(\cos\left(\alpha+\varphi_{\mathrm{u}2j}\right) - \cos\left(\alpha+\varphi_{\mathrm{u}2j}+\mu\right)\right)\right] \tag{A21}$$

Assume that overlap angle μ is very small,

$$\begin{aligned} i_{\mathrm{dc}} &= \frac{\sqrt{3}}{2\omega_0}\left[\begin{array}{l} \dfrac{U_3}{L_3}\left(\cos\left(\alpha\right) - \cos\left(\alpha\right)\cos\left(\mu\right) + \sin\left(\alpha\right)\sin\left(\mu\right)\right) \\ +\dfrac{U_2}{L_2}\left(\cos\left(\alpha+\varphi_{\mathrm{u}2j}\right) - \cos\left(\alpha+\varphi_{\mathrm{u}2j}\right)\cos\left(\mu\right) + \sin\left(\alpha+\varphi_{\mathrm{u}2j}\right)\sin\left(\mu\right)\right) \end{array}\right] \\ &= \frac{\sqrt{3}}{2\omega_0}\left[\begin{array}{l} \dfrac{U_3}{L_3}\left(\cos\left(\alpha\right)\left[1-\cos\left(\mu\right)\right] + \sin\left(\alpha\right)\sin\left(\mu\right)\right) \\ +\dfrac{U_2}{L_2}\left(\cos\left(\alpha+\varphi_{\mathrm{u}2j}\right)\left[1-\cos\left(\mu\right)\right] + \sin\left(\alpha+\varphi_{\mathrm{u}2j}\right)\sin\left(\mu\right)\right) \end{array}\right] \\ &\approx \frac{\sqrt{3}}{2\omega_0}\left[\frac{U_3}{L_3}\left(\sin\left(\mu\right)\sin\left(\alpha\right)\right) + \frac{U_2}{L_2}\left(\sin\left(\mu\right)\sin\left(\alpha+\varphi_{\mathrm{u}2j}\right)\right)\right] \\ &= \frac{\sqrt{3}}{2\omega_0}\sin\left(\mu\right)\left[\frac{U_3}{L_3}\sin\left(\alpha\right) + \frac{U_2}{L_2}\sin\left(\alpha+\varphi_{\mathrm{u}2j}\right)\right] \end{aligned} \tag{A22}$$

Treating Eq. (A22) as an equation in μ yields Eq. (15).

Appendix C

Discussion on the impact of nominal tolerances on robustness:

The paper assumes that the nominal tolerance of the components is within ±10%.

In the calculation formula for the SVF bridge arm current boundary $|i_{2j}|$ (Eq. (8)), the expression consists of three terms. Based on the parameter settings in this paper, the maximum relative error of the first term in Eq. (8) is calculated as follows:

$$\begin{aligned}
&\max\left(\sqrt{\left[-\frac{1}{\omega_0\left(\left(\hat{L}_2+\hat{L}_3\right)\right)}\eta_j U_3+\frac{1}{\omega_0\left(\hat{L}_2+\hat{L}_3\right)}U_2\cos\left(\varphi_{u2j}\right)\right]^2+\left[\frac{1}{\omega_0\left(\hat{L}_2+\hat{L}_3\right)}U_2\sin\left(\varphi_{u2j}\right)\right]^2}\right)\\
&-\sqrt{\left[-\frac{1}{\omega_0\left(L_2+L_3\right)}\eta_j U_3+\frac{1}{\omega_0\left(L_2+L_3\right)}U_2\cos\left(\varphi_{u2j}\right)\right]^2+\left[\frac{1}{\omega_0\left(L_2+L_3\right)}U_2\sin\left(\varphi_{u2j}\right)\right]^2}\\
&\sqrt{\left[-\frac{1}{\omega_0\left(L_2+L_3\right)}\eta_j U_3+\frac{1}{\omega_0\left(L_2+L_3\right)}U_2\cos\left(\varphi_{u2j}\right)\right]^2+\left[\frac{1}{\omega_0\left(L_2+L_3\right)}U_2\sin\left(\varphi_{u2j}\right)\right]^2}\times 100\%\\
&=\frac{\frac{1}{0.9\left(L_2+L_3\right)}-\frac{1}{\left(L_2+L_3\right)}}{\frac{1}{\left(L_2+L_3\right)}}\times 100\%\approx 11.1\%
\end{aligned}\tag{A23}$$

The superscript '∧' denotes the actual value.

The maximum relative error of the second term in Eq. (8) is calculated as follows:

$$\begin{aligned}
&\frac{\max\left(\frac{\hat{L}_3}{\hat{L}_2+\hat{L}_3}i_{dc}\right)-\frac{L_3}{L_2+L_3}i_{dc}}{\frac{L_3}{L_2+L_3}i_{dc}}\times 100\%\\
&=\frac{\max\left(\frac{1}{1+\hat{L}_2/\hat{L}_3}\right)-\frac{L_3}{L_2+L_3}}{\frac{L_3}{L_2+L_3}}\times 100\%\\
&=\frac{\frac{1}{1+\frac{0.0085}{0.015}\times\frac{0.9}{1.1}}-\frac{0.015}{0.0085+0.015}}{\frac{0.015}{0.0085+0.015}}\times 100\%\\
&\approx 7.04\%
\end{aligned}\tag{A24}$$

Since the second term is generally larger than the first term, after averaging the two terms, the error of $|i_{2j}|$ is typically within 10%.

Given that a 22% margin is applied to the current blocking threshold I_{permit}, the maximum possible current over-limit due to these errors is

$$1.1I_{\text{permit}} = 1.1 \times 0.783I_{\text{CRM}} = 86.3\%I_{\text{CRM}} \tag{A25}$$

This will not cause device damage.

Similarly, the maximum relative error of the SVF capacitor voltage (Eq. (12)) is

$$\left(\frac{L_3}{\left(\frac{0.9}{1.1}L_2 + L_3\right) \cdot 0.9C_f} \Big/ \frac{L_3}{(L_2 + L_3) \cdot C_f} - 1 \right) \times 100\% = 18.9\% \tag{A26}$$

Consequently, the maximum submodule voltage is

$$(1 + 1.189\xi)\, U_{\text{C}} = (1 + 1.189 \times 0.26)\, U_{\text{C}} = 1.3U_{\text{C}} \tag{A27}$$

The submodule maximum allowable capacitor voltage is set precisely at $1.3U_{\text{C}} = 3640$V. Considering that the approximation for $|\Delta u_{\text{C}}|$ is an overestimation, the actual value of $|\Delta u_{\text{C}}|$ will be smaller than the calculated value, thereby still preventing device damage.

This also will not cause device damage.

However, under the most severe conditions, the protection may be triggered inadvertently.

Observing the expression of V_{m1} (Eq. (17)), it is evident that, due to nominal parameter tolerances of the devices, its actual desired value becomes 0.9 V_{m1}.

The actual desired value of V_{m2} (Eq. (19)):

$$\begin{aligned} \wedge V_{\text{m2}} &= \frac{\dfrac{\left(\hat{L}_2 + \hat{L}_3\right)\hat{C}_{\text{f}} u_{\text{dc}} \omega_0 N_{\text{sub}} \xi U_{\text{c}}}{\hat{L}_3 I_{\text{dc}}} - \dfrac{(L_2 + L_3)\, C_{\text{f}} u_{\text{dc}} \omega_0 N_{\text{sub}} \xi U_{\text{c}}}{L_3 I_{\text{dc}}}}{\dfrac{(L_2 + L_3)\, C_{\text{f}} u_{\text{dc}} \omega_0 N_{\text{sub}} \xi U_{\text{c}}}{L_3 I_{\text{dc}}}} V_{\text{m2}} \\ &= \frac{\left(\dfrac{0.9}{1.1}\dfrac{L_2}{L_3} + 1\right), 0.9C_{\text{f}}}{\left(\dfrac{L_2}{L_3} + 1\right) C_{\text{f}}} V_{\text{m2}} = 0.84V_{\text{m2}} \end{aligned} \tag{A28}$$

Therefore, in practical engineering applications, two safety factors (A_1, A_2) can be applied to the feedforward coefficient K_{v} (Eq. (20)).

That is

$$K_{\text{v}} = \frac{\min\left(A_1 V_{\text{m1}}, A_2 V_{\text{m2}}\right) - U_2}{U_3} \tag{A29}$$

where, A_1 is the maximum allowable tolerance of inductance nominal error, and the calculation of A_2 refers to Eq. (A28).

References

1. Xiao H, Sun K, Pan J, Li Y, Liu Y. Review of hybrid HVDC systems combining line communicated converter and voltage source converter. Int J Electr Power Energy Syst. 2021;129(2):106713. doi:10.1016/j.ijepes.2020.106713.
2. Sun X, Liu Z, Gao L, Ding Y. Practice and innovation in the ±800 kV UHVDC demonstration project. Proc CSEE. 2009;29:35–45.
3. Yakupoğlu H, Gozde H, Taplamacıoğlu M. Technical and economic comparison of Hvdc converter technologies. Int J Tech Phys Probl Eng. 2018;10(37):25–30.
4. Shi Z, Wang W, Huang Y, Li P, Dong L. Simultaneous optimization of renewable energy and energy storage capacity with the hierarchical control. CSEE J Power Energy Syst. 2022;8(1):95–104. doi:10.17775/CSEEJPES.2019.01470.
5. Anonymous. A Review of LCC-HVDC and VSC-HVDC technologies and applications|IEEE conference publication|IEEE Xplore. n.d. [cited 2025 Nov 17]. Available from: https://ieeexplore.ieee.org/document/7555677.
6. Sun K, Hou Y, Sun W, Qi J. Emerging technologies in system restoration. In: Power system control under cascading failures: understanding, mitigation, and system restoration. New York, NY, USA: IEEE; 2019. p. 357–97. doi:10.1002/9781119282075.ch9.
7. Fernandes RO, Tavares MCD. Mitigation of the commutation failure problem in the HVDC multi-infeed scenario in Brazil using synchronized phasor measurement. Electr Power Syst Res. 2024;235(1):110829. doi:10.1016/j.epsr.2024.110829.
8. Ahrabi RR, Li YW, Nejabatkhah F. Hybrid AC/DC network with parallel LCC-VSC interlinking converters. IEEE Trans Power Syst. 2021;36(1):722–31. doi:10.1109/tpwrs.2020.3020235.
9. Wu S, Qi L, Jin M, He Z, Zhang X. An MMC with integrated energy dissipation function using thyristor-based chopper modules for the offshore wind VSC-HVDC system. IEEE Trans Power Electron. 2024;39(1):1609–23. doi:10.1109/tpel.2023.3322986.
10. Alam MS, Hossain MA, Shafiullah M, Islam A, Choudhury MSH, Faruque MO, et al. Renewable energy integration with DC microgrids: challenges and opportunities. Electr Power Syst Res. 2024;234(6):110548. doi:10.1016/j.epsr.2024.110548.
11. Pinto Fernandes R, Lucas Lirio F, César de Oliveira B, Carlos Siqueira de Lima A. Performance comparison of LCC and VSC HVDC systems in minimizing long-term voltage collapse. IEEE Access. 2025;13(37):53965–79. doi:10.1109/access.2025.3554448.
12. Mejia-Ruiz GE, Paternina MRA, Qu Z, Ahmed S, Konstantinou C. Multiple ancillary services provision by optimal control of aggregated inverter-based resources. Int J Electr Power Energy Syst. 2025;171(2):110953. doi:10.1016/j.ijepes.2025.110953.
13. Mejia-Ruiz GE, Cardenas-Javier R, Arrieta Paternina MR, Rodriguez-Rodriguez JR, Ramirez JM, Zamora-Mendez A. Coordinated optimal volt/var control for distribution networks via D-PMUs and EV chargers by exploiting the eigensystem realization. IEEE Trans Smart Grid. 2021;12(3):2425–38. doi:10.1109/tsg.2021.3050443.
14. Ma W, Wang L, Li M, Shen X, Wu F, Xu Y. SLCC converter technology of UHVDC transmission in new power system. High Volt Eng. 2022;48(12):4941–8. doi:10.13336/j.1003-6520.hve.20220760.
15. Jia G, Liu Z, Zhang Z, Chen M, Xu F, Niu F. Research on operation control strategy of self-adaption statcom and line commutation converter. Proc CSEE. 2025;45(12):4843–58. doi:10.13334/j.0258-8013.pcsee.241053.
16. Deng X. Research on the application of SVG in LCC-HVDC [master's thesis]. Beijing, China: North China Electric Power University; 2025. doi:10.27140/d.cnki.ghbbu.2024.001759.
17. Liao S, Gan D, Shi Z. A study on HVDC overcurrent during commutation failure. IEEE Trans Power Deliv. 2024;39(3):1963–74. doi:10.1109/tpwrd.2024.3384572.
18. Liu Z, Yu J, Guo X, Sun T, Zhang J. Survey of technologies of line commutated converter based high voltage direct current transmission in China. CSEE Power and Energy Syst. 2015;1(2):1–8. doi:10.17775/cseejpes.2015.00014.
19. Nian H, Liu Y, Li H, Hu B, Liao Y, Yang J. Commutation overlap characteristic modeling and stability analysis of LCC-HVDC in sending AC grid. IEEE Trans Sustain Energy. 2022;13(3):1594–606. doi:10.1109/tste.2022.3167106.
20. Liu L, Lin S, Sun P, Liao K, Li X, Deng Y, et al. A calculation method of pseudo extinction angle for commutation failure mitigation in HVDC. IEEE Trans Power Deliv. 2019;34(2):777–9. doi:10.1109/tpwrd.2019.2892613.

21. Wei Z, Fang W, Liu J. Variable extinction angle control strategy based on virtual resistance to mitigate commutation failures in HVDC system. IEEE Access. 2020;8:93692–704. doi:10.1109/access.2020.2994245.
22. Liu B, Chen Z, Yang S, Lu C, Deng X, Wang R. Research on methods of measuring extinction angle and measures to suppress repetitive commutation failures through equivalent DC input resistance. Int J Electr Power Energy Syst. 2021;133(1):107326. doi:10.1016/j.ijepes.2021.107326.
23. Zhu R, Zhou X, Xia H, Hong L, Yin H. A commutation failure prediction and mitigation method. J Mod Power Syst Clean Energy. 2022;10(3):779–87. doi:10.35833/mpce.2020.000771.